

# The HIX galaxy survey II: HI kinematics of HI eXtreme galaxies

K. A. Lutz,<sup>1,2\*</sup> V. A. Kilborn,<sup>1</sup> B. S. Koribalski,<sup>2</sup> B. Catinella,<sup>3</sup>  
 G. I. G. Józsa,<sup>4,5,6</sup> O. I. Wong,<sup>3</sup> A. R. H. Stevens,<sup>1,3</sup> D. Obreschkow,<sup>3</sup>  
 H. Dénes,<sup>2,7</sup>

<sup>1</sup> Centre for Astrophysics and Supercomputing, Swinburne University of Technology, P.O. Box 218, Hawthorn, VIC 3122, Australia

<sup>2</sup> Australia Telescope National Facility, CSIRO Astronomy and Space Science, P.O. Box 76, Epping, NSW 1710, Australia

<sup>3</sup> International Centre for Radio Astronomy Research (ICRAR), M468, The University of Western Australia, 35 Stirling Highway, Crawley, WA 6009, Australia

<sup>4</sup> SKA South Africa Radio Astronomy Research Group, 3rd Floor, The Park, Park Road, Pinelands 7405, South Africa

<sup>5</sup> Rhodes Centre for Radio Astronomy Techniques & Technologies, Department of Physics and Electronics, Rhodes University, PO Box 94, Grahamstown 6140, South Africa

<sup>6</sup> Argelander-Institut für Astronomie, Auf dem Hügel 71, D-53121 Bonn, Germany

<sup>7</sup> Research School of Astronomy and Astrophysics, The Australian National University, Canberra, ACT 2611, Australia

Accepted XXX. Received YYY; in original form ZZZ

## ABSTRACT

By analysing a sample of galaxies selected from the HI Parkes All Sky Survey (HIPASS) to contain more than 2.5 times their expected HI content based on their optical properties, we investigate what drives these HI eXtreme (HIX) galaxies to be so HI-rich. We model the HI kinematics with the *Tilted Ring Fitting Code* TiRiFiC and compare the observed HIX galaxies to a control sample of galaxies from HIPASS as well as simulated galaxies built with the semi-analytic model DARK SAGE. We find that (1) HI discs in HIX galaxies are more likely to be warped and more likely to host HI arms and tails than in the control galaxies, (2) the average HI and average stellar column density of HIX galaxies is comparable to the control sample, (3) HIX galaxies have higher HI and baryonic specific angular momenta than control galaxies, (4) most HIX galaxies live in higher-spin haloes than most control galaxies. These results suggest that HIX galaxies are HI-rich because they can support more HI against gravitational instability due to their high specific angular momentum. The majority of the HIX galaxies inherits their high specific angular momentum from their halo. The HI content of HIX galaxies might be further increased by gas-rich minor mergers.

This paper is based on data obtained with the Australia Telescope Compact Array (ATCA) through the large program C 2705.

**Key words:** galaxies – evolution, galaxies – formation, galaxies – kinematics and dynamics, galaxies – ISM

## 1 INTRODUCTION

The gaseous and stellar content of galaxies is tightly related through the galactic gas cycle. Atomic hydrogen (HI) condenses to form molecular gas (H<sub>2</sub>) clouds. These clouds are the birth places of stars. When comparing the amount of available HI to the current star formation rate in local galaxies, Kennicutt (1998) and Schiminovich et al. (2010) find that their HI reservoirs would be consumed within  $\approx 2$  Gyr.

Hence, galaxies need to replenish their gas reservoir in order to remain active starformers in the future (Sancisi et al. 2008, Sánchez Almeida et al. 2014 and references therein).

Gas-rich mergers and smooth accretion from the circumgalactic medium are suggested as avenues for gas replenishment (White & Rees 1978). Observations of local galaxies do not find evidence for enough gas rich mergers to sustain star formation (Di Teodoro & Fraternali 2014; Sancisi et al. 2008; Sánchez Almeida et al. 2014). This leads to the conclusion that smooth accretion is the dominant channel of gas accretion. This might be the reaccretion of gas previ-

\* E-mail: research@katha-lutz.de

ously ejected by feedback mechanisms together with pristine halo gas, which is dragged along (à la the “Galactic Fountain”, see e.g. Oosterloo et al. 2007; Fraternali et al. 2011). Cosmological simulations suggest accretion occurs through the cooling of hot halo gas or through the delivery of cold gas through filaments (Birnboim & Dekel 2003; Kereš et al. 2005; Dekel & Birnboim 2006; van de Voort et al. 2011). In the local Universe, gas-phase metallicity gradients / inhomogeneities (Moran et al. 2012), warps (Roškar et al. 2010) and lopsided discs (Bournaud et al. 2005) may be interpreted as observations of cosmological accretion but may also result from tidal interactions with other galaxies.

The HALOGAS survey (Heald et al. 2011) has previously searched for signs of accretion in deep H I observations of nearby galaxies (distance < 11 Mpc). Through detailed modelling of the H I kinematics, the HALOGAS team has found a few high velocity clouds, thick H I discs, and warps in their samples galaxies (Gentile et al. 2013; Zschaechner et al. 2011, 2012; de Blok et al. 2014). In the Milky Way, high velocity clouds are thought to contribute to gas accretion (Putman et al. 2012). The thick disc component, which is usually lagging in rotation velocity with respect to the thin disc, is interpreted as a sign of the Galactic Fountain (Oosterloo et al. 2007; Fraternali et al. 2011). However, the total rate of detected H I accretion in the HALOGAS observations is not sufficient to fuel star formation in their sample galaxies (Heald 2015).

The H I eXtreme (HIX) galaxy survey examines a sample of H I-rich galaxies to understand how they accumulate and maintain their gas reservoirs. In Lutz et al. (2017), we found that HIX galaxies are less efficient at forming stars than a control sample. The most extreme galaxy in the HIX sample (ESO075-G006) has built its massive H I disc through a combination of a lower star formation efficiency ( $SFE_{\text{HI}} = \text{SFR}/M_{\text{HI}}$ ), due to a high specific baryonic angular momentum, and likely some accretion of pristine gas (as probed by gas-phase metallicity gradients).

So the gas-rich galaxies of the HIX survey are not necessarily gas-rich due to recent gas accretion but could also be inefficient at using their available gas for star formation. Simple models describing the H I based star formation efficiency ( $SFE_{\text{HI}} = \text{SFR}/M_{\text{HI}}$ ) find a strong dependence of the SFE on the stability of the disc (Wong et al. 2016). Maddox et al. (2015) suggests that the upper envelope of the stellar – H I mass relation at high stellar masses is defined by the halo spin parameter. That is galaxies with a high H I mass for their stellar mass tend to live in higher spin haloes. A high angular momentum can reduce the star formation efficiency in two ways: (1) accreted gas can not be transported to the denser, inner parts of the galaxy (Kim & Lee 2013; Forbes et al. 2014), where the star formation efficiency would be higher (Leroy et al. 2008); (2) the disc is stabilised against star formation (Toomre 1964; Obreschkow et al. 2016).

In this paper, we extend the analysis of the relation between the H I content and kinematic properties to the entire HIX sample and an accompanying control sample. We make use of observations of our sample galaxies with the Australia Telescope Compact Array (ATCA), which provide spatially resolved H I distributions and kinematics.

This article is structured as follow. In Sec. 2, we discuss the selection of the HIX and control samples and present the data used in this paper. In Sec. 3, we present the results

of the analysis of H I kinematics and distribution. We then compare our results to the semi-analytic model DARK SAGE of galaxy evolution in Sec. 4. The results are discussed in Sec. 5. We then conclude in Sec. 6.

Throughout the paper we will assume a flat  $\Lambda$ CDM cosmology with the following cosmological parameters:  $H_0 = 70.0 \text{ km Mpc}^{-1} \text{ s}^{-1}$ ,  $\Omega_m = 0.3$ . All velocities are used in the optical convention (cz).

## 2 SAMPLES AND DATA

### 2.1 Galaxy samples

In this paper, we perform a kinematic analysis of galaxies in the HIX survey, which was first presented in Lutz et al. (2017). HIX galaxies were selected as a subsample of the compilation presented by Dénes et al. (2014), who used their sample to calibrate scaling relations between H I mass and optical luminosity. This parent sample consists of 1796 galaxies from the HIPASS catalogues (Meyer et al. 2004; Koribalski et al. 2004), which have reliable optical counterparts in HOPCAT (Doyle et al. 2005).

In our 2017 paper, HIX and control samples included 13 galaxies each. HIX galaxies were selected to lie at least  $1.4\sigma$  above the Dénes et al. (2014) scaling relation between H I mass and absolute  $R$ -band magnitude. The control sample has been selected from the same parent sample to lie within  $\pm 0.7\sigma$  of the scaling relation. We exclude dwarf galaxies by restricting our sample to stellar masses greater than  $\log M_{\star} [M_{\odot}] > 9.7$ . In this paper, control galaxies NGC 4672, IC 4366 and ESO462-G016 are excluded because the signal to noise ratio of their H I data was too low.

For ESO208-G026 and IC 4857 the last paper was inconclusive on whether these two galaxies are true HIX galaxies, because in the H I mass fraction vs. stellar mass plane, both galaxies were located within the  $1\sigma$  scatter of the HIPASS parent sample (see below in Fig. 1). Upon examination of the HOPCAT aperture that was used to measure the optical photometry of IC 4857, it became apparent that a spiral arm to the east of the galaxy had not been included in the photometrical analysis. This led to an underestimation of the  $R$ -band magnitude and subsequently an overestimation of the H I-richness. IC 4857 is therefore reclassified as a control galaxy. As will be seen in the analysis of this paper, the properties of the H I disc of IC 4857 are furthermore similar to the remaining control sample and not to the HIX sample. Neither the analysis of the optical/near-infrared photometry nor of the resolved H I observations of ESO208-G026 were able to explain why this galaxy is a clear outlier on the Dénes et al. (2014) relation but not as much on the H I mass fraction vs. stellar mass plane. Therefore, ESO208-G026 remains in the HIX sample.

### 2.2 Ancillary data

Information on the stellar content of the HIX and control galaxies is based on data from the 2Micron All Sky Survey (2MASS) and the associated Extended Source Catalogue (2MASX, Skrutskie et al. 2006). Stellar masses are calculated from the total 2MASX  $K$ -band magnitude following

equ. 3 of Wen et al. (2013):

$$\log M_{\star} [M_{\odot}] = -0.498 + 1.105 \times \log L_K [L_{\odot}]. \quad (1)$$

Only 1478 out of the 1796 galaxies in the parent sample have a cross match in the 2MASX catalogue (82 per cent). These “missing” galaxies are excluded from the analysis.

In section 3.3, we will consider the atomic gas mass  $M_A$  and the baryonic mass  $M_B$ . We define these masses as follows:

$$M_A = M_{\text{HI}+\text{He}} = 1.35 M_{\text{HI}} \quad (2)$$

i. e. the H I mass with a correction factor to account for Helium (e. g. Obreschkow et al. 2016) and

$$M_B = M_A + M_{\star}. \quad (3)$$

where  $M_{\star}$  is the stellar mass. We neglect the molecular gas mass in this calculation of the baryonic mass, because the ISM of HIX and control galaxies is dominated by atomic gas and estimated molecular gas masses (e. g. using scaling relations by Catinella et al. (2010) and Saintonge et al. (2011)) are an order of magnitude smaller than atomic gas masses.

### 2.3 Resolved HI data from ATCA

For this paper we focus on the H I interferometric data of the HIX and control sample. All data has been obtained with the Australia Telescope Compact Array (ATCA). While the majority of the observations for the HIX galaxies have been carried out as part of the large program C 2705, the data of the control sample has been collected from the Australia Telescope Online Archive (ATOA)<sup>1</sup>. Table 1 summarises all ATCA observations that will be used in this paper.

Since 2009, the ATCA is equipped with the Compact Array Broadband Backend (CABB, Wilson et al. 2011). All observations after 2009 used CABB but depending on the observing project, CABB has been used in two different modes: CFB 1M-0.5k (0.5 kHz resolution) and CFB 64M-34k mode (34 kHz resolution, used in project C 2921). All observations prior to 2009 were obtained with the previous correlator (16 kHz resolution).

The methodology of the data reduction is similar for all three set-ups, and a semi-automated MIRIAD pipeline is used in all cases. Firstly, radio frequency interference (e. g. signal from GPS Satellites) is removed. A semi-automated pipeline conducts bandpass, flux, and phase calibration using the MIRIAD (Sault et al. 1995) tasks GPCAL and MFBOOT. For bandpass and flux calibration the standard calibration source PKS 1934-638 has been observed before or after each galaxy observation. The phase calibrator is given in Tab. 1 and has been visited regularly during the galaxy observations. The calibration is then applied to the galaxy data. In the final step of the pipeline, a first-order polynomial baseline is subtracted from each galaxy observation. We consider the results of this procedure satisfactory, once the phase of the phase calibrator is tightly scattered around 0 across the observing period and the amplitudes of the phase and bandpass calibrators are in agreement with the ATCA calibrator data base.<sup>2</sup>

A second pipeline combines all available observations of one galaxy from different array configurations in the Fourier transformation. For this step, the MIRIAD task INVERT is used. The obtained dirty data cube is then cleaned (CLEAN), restored (RESTOR) and primary beam corrected (LINMOS). Mosaicking is necessary in one case, where data has been compiled from different observing projects (NGC 289). In this case cleaning is carried out with MOSSDI and no primary beam correction is necessary.

Moment 0, 1 and 2 maps are created with the MIRIAD task MOMENT. A three-sigma clipping is applied. Furthermore, values in the moment 1 maps are restricted such that only velocities that can be measured with our correlator set-up are included. Both options reduce the noise in the resulting maps. Moment 1 and 2 maps are then masked to regions where the column density in the moment 0 maps is larger than  $0.4$  and  $0.8 \times 10^{20} \text{ cm}^{-2}$  for HIX and control sample, respectively. In addition, moment 0 maps without the three-sigma clipping are created.

Within the errors, the H I masses as measured from the ATCA H I data cubes and the H I masses as measured from the integrated flux from the HIPASS catalogues agree for all HIX galaxies and for half of the control galaxies. In the appendices, a HIPASS spectrum is given, which has been re-measured from the HIPASS data cubes. Due to different baselines, the H I masses as measured from the ATCA H I data cubes and as re-measured from HIPASS data cubes only agree within the errors for 83 and 43 per cent of the HIX and the control galaxies, respectively.

The different column density limits and flux recovery percentages are due to the fact that the HIX observations are, in general, more sensitive than the control galaxy observations because of:

- longer total on-source integration times for the HIX galaxies.
- higher system temperature of the old correlator, which was used for most of the control sample observations.

For most results in this paper, the different limits do not pose a problem because:

- (i) all extended features in the HIX galaxies that are relevant in our analysis are also detected at column densities  $> 0.8 \times 10^{20} \text{ cm}^{-2}$ .
- (ii) the H I radius is measured at  $1 M_{\odot} \text{ pc}^{-2} = 1.2 \times 10^{20} \text{ cm}^{-2}$  (see Sec. 2.5), well above both detection limits.

It is, however, to be noted that the observations of control galaxies generally include fewer short baselines than the observations of HIX galaxies. Hence, some diffuse features in control galaxies may be missed in this analysis. This problem may only be resolved with significant amounts of new data. For example, arms and tails as found in HIX galaxies ESO381-G005 and ESO208-G026 are only detected once we at least combine observations from the 1.5 km and the 750 m array configuration. When only using 1.5 km array configuration observations, we are able to detect the tail in ESO378-G003 but not the associated cloud in this galaxy or any arms in ESO381-G005 and ESO208-G026 (see Sec. 3.2 for more details). The combination of observations of the 1.5 km and the 750 m array configuration is only available for six out of eleven control galaxies.

Table 2 summarises the characteristics of the final data

<sup>1</sup> <http://atoa.atnf.csiro.au/>

<sup>2</sup> <http://www.narrabri.atnf.csiro.au/calibrators/>

ID (1)	1.5km Array (2)	750m Array (3)	EW Array (4)	$t_{\text{OS}}$ [h] (5)	Phase Calibrator (6)	$f_{\text{Cen}}$ [MHz] (7)
ESO111-G014	2012-12-19	2013-01-20	2013-01-16	24.6	2355-534	1384
ESO243-G002	2015-06-15	...	2012-11-08	17.9	0022-423	1378
NGC 289	2002-07-06 <sup>(a)</sup>	2015-09-07	2015-08-28	27.7	0022-423 / 0042-357	1413
ESO245-G010	2014-11-16	2015-02-24	2014-11-29	20.9	0201-440	1393
ESO417-G018	2014-11-14	2015-09-08	2014-11-30 2012-05-07	20.1	0237-233 / 0153-410	1398
ESO055-G013	2014-11-15	2015-02-24	2014-12-01	21.6	0252-712	1385
ESO208-G026	2014-11-17	2015-09-10	2015-08-29	29.5	0823-500	1406
ESO378-G003	2015-06-13	2015-09-09	2015-08-31	28.3	1144-379	1406
ESO381-G005	2015-06-14	2015-09-07	2015-08-31	28.4	1232-416	1394
ESO461-G010	2014-11-14	2015-02-23	...	13.6	1921-293	1389
ESO075-G006	2012-12-20	2013-01-19	2012-11-08	20.5	1934-638	1370
ESO290-G035	2014-11-15	2015-02-14	2014-11-30 2012-05-08	20.3	2333-528	1392
NGC 685	1995-10-29 <sup>(b)</sup>	1995-09-30 <sup>(b)</sup>	...	20.0	0407-658	1414
ESO121-G026	2014-05-13 <sup>(c)</sup>	...	...	10.9	0539-530	1396
ESO123-G023	2001-08-04 <sup>(d)</sup>	2000-05-10 <sup>(d)</sup>	...	20.0	0727-365	1407
NGC 3001	2014-05-12 <sup>(c)</sup>	...	...	11.1	0919-260	1396
ESO263-G015	2001-03-15 <sup>(e)</sup>	...	...	10.8	1039-47	1408
NGC 3261	1997-05-01 <sup>(f)</sup>	1997-06-09 <sup>(f)</sup>	1997-04-02 <sup>(f)</sup>	30.0	0823-500 / 1215-457	1407
NGC 5161	2014-05-14 <sup>(c)</sup>	...	...	10.5	1255-316	1396
ESO383-G005	2000-05-20 <sup>(g)</sup>	...	...	9.8	1320-446	1403
IC 4857	2015-06-17	2015-09-05	2012-06-06	20.4	1934-638	1399
ESO287-G013	2001-10-28 <sup>(d)</sup>	2000-05-09 <sup>(d)</sup>	...	20.6	2106-413	1408
ESO240-G011	2001-07-28 / 29 <sup>(d)</sup>	2000-05-11 <sup>(d)</sup>	...	19.9	2326-477	1407

**Table 1.** The ATCA H I observations used in this paper. Observations listed above the horizontal line belong to HIX galaxies, below to control galaxies. *Column* (1): Galaxy ID as defined in [Dreyer \(1888, 1910\)](#); [Lauberts & Valentijn \(1989\)](#). *Column* (2), (3) and (4): Date of observation in any 1.5 km, 750m and EW array configuration. *Column* (5): On source observation time in hours. *Column* (6): Phase Calibrator PKS [ID number] (based on the Parkes Catalogue ([Wright & Otrupcek 1990](#)) and its predecessors). *Column* (7): Central frequency of band in MHz. Most HIX galaxy observations have been observed in the project C 2705. More observations are taken from the following projects: <sup>(a)</sup> C 819, <sup>(b)</sup> C 473, <sup>(c)</sup> C 2921, <sup>(d)</sup> C 885, <sup>(e)</sup> C 869, <sup>(f)</sup> C 633 and <sup>(g)</sup> C 801.

cubes of each galaxy. The rms of the data cubes is around 1 to 3 mJy beam<sup>-1</sup>. Beam sizes range between 65 by 43 arcsec and 25 by 18 arcsec.

## 2.4 TiRiFiC modelling

We use the Tilted RInG Flitting Code TiRiFiC ([Józsa et al. 2007](#)) to analyse the kinematic properties of HIX and control galaxies. The tilted ring fitting method has first been introduced by [Rogstad et al. \(1974\)](#) and allows one to measure rotation velocity, position angle, inclination and more properties in concentric annuli.

In the case of the HIX and control sample we consider the following two models:

- a flat disc (FLAT). In this case only the surface brightness and the rotation curve are allowed to vary with radius. All other parameters like inclination, position angle, centre of rotation, velocity dispersion, thickness of the disc and systemic velocity are the same in all rings.
- a warped disc with radius-dependent inclination and position angle (WARP).

The inclination and position angle within the optical  $B_j$ -band 25 mag arcsec<sup>-2</sup> isophotal radius ([Lauberts & Valentijn 1989](#)) are kept constant regardless of the model to be fitted, because the optical discs of both the HIX and the control sample do not appear warped upon visual inspection (see e. g. the approach to model NGC 4414 by [de Blok et al. 2014](#)). This means that position angle and inclina-

tion are fitted simultaneously for all rings within the optical 25 mag arcsec<sup>-2</sup> isophotal radius.

The width of the rings is of the order of the beam size, and rings with smaller widths are introduced at small radii. The number of rings is chosen such that the outermost ring is the first one without emission.

To avoid over-interpreting our data, we did not fit more parameters like, for example, a vertical lag in rotation velocity, which might indicate an active Galactic Fountain (as described in Sec. 1). Our sample galaxies are located at distances between 18 Mpc and 148 Mpc, which is two to ten times further away than the HALOGAS galaxies. Therefore, one resolution element covers a larger fraction of the galaxy than was the case for HALOGAS galaxies. The TiRiFiC modelling does, however, include the geometrical “Z0” parameter, which is the thickness of the disc.

For every galaxy in the control and HIX sample, we chose a final TiRiFiC model by:

- visual inspection of channel maps of the input data cube and the output model cube.
- aiming for radially smooth variations (if any) of rotation velocity, inclination and position angle.
- minimising the free parameters that are fitted. That means, if a flat disc model and a warped disc model produce similarly small residuals we will chose the flat disc model.

ID	$\theta_1$	$\theta_2$	rms
(1)	[ $''$ ]	[ $''$ ]	[mJy beam $^{-1}$ ]
(1)	(2)	(3)	(4)
ESO111-G014	52.66	40.58	1.7
ESO243-G002	31.70	22.95	1.5
NGC 289 <sup>a</sup>	55.98	25.64	1.4
ESO245-G010	51.48	31.30	1.7
ESO417-G018	66.09	33.33	1.6
ESO055-G013	43.08	33.54	2.0
ESO208-G026	59.24	43.49	1.3
ESO378-G003	64.23	41.09	1.3
ESO381-G005	65.76	43.50	1.5
ESO461-G010 <sup>b</sup>	59.62	29.38	2.7
ESO075-G006	60.52	35.22	2.0
ESO290-G035 <sup>b</sup>	58.32	28.98	2.1
NGC 685	34.58	32.48	1.9
ESO121-G026 <sup>c</sup>	25.42	18.91	0.6
ESO123-G023	35.74	28.94	2.3
NGC 3001 <sup>c</sup>	38.49	20.97	1.3
ESO263-G015	25.53	22.60	3.0
NGC 3261	56.50	39.31	2.7
NGC 5161 <sup>c</sup>	36.59	20.41	1.3
ESO383-G005	40.83	22.02	2.8
IC 4857	40.16	26.92	1.1
ESO287-G013	38.00	30.33	2.0
ESO240-G011	29.32	22.87	3.0

**Table 2.** Characteristics of the final data cubes for HIX (above horizontal line) and control galaxies (below horizontal line). *Column* (1): Galaxy ID. *Column* (2): Beam major axis in arcsec. *Column* (3): Beam minor axis in arcsec. *Column* (4): RMS in the final data cube. The weighting is set by the robust parameter in MIRIAD’s INVERT task. A weighting of 2.0 indicates natural weighting and a weighting of -2.0 corresponds to uniform weighting. For most cubes a weighting with robust=0.5 was chosen except for <sup>a</sup> and <sup>b</sup> where robust = 2.0 and 0.0 was chosen respectively. <sup>c</sup> indicates that the data cube has a velocity channel width of 6 km s $^{-1}$  instead of 4 km s $^{-1}$ .

As output, TiRiFiC provides a model data cube and a table with the radial profiles of the fitted parameters.

## 2.5 Radial profiles

The radial profiles of the H I column density, H I mass and stellar mass are measured using the radial profiles of inclination and position angle from TiRiFiC. In a first step we extrapolate inclination and position angle between the TiRiFiC rings. Then concentric, elliptical annuli are defined. The width of these annuli is of the order of the pixel size. Inclination and position angle of each annulus are taken from the extrapolated TiRiFiC profiles according to their radius. Within each elliptical annulus, we measure the total H I mass, the total stellar mass and the average H I column density. H I mass and column density profiles are measured from the non-clipped moment 0 maps and stellar mass profiles from the 2MASS *K*-band images. The 2MASS luminosities in every annulus are converted to stellar masses again using equ. 3 of Wen et al. (2013) (see Equ. 1). Stellar masses are only determined in annuli, which are smaller than the aperture within which 2MASS measured the integrated *K*-band magnitude.

TiRiFiC also provides rotation velocities for each fitted ring. These rotation velocities are fitted with a rotation

curve of the functional form:

$$V_{\text{rot}}(r) = V_{\text{flat}} \cdot \left[ 1 - \exp\left(\frac{-r}{l_{\text{flat}}}\right) \right] \quad (4)$$

(Leroy et al. 2008 and references therein).  $V_{\text{flat}}$  is the circular velocity in the flat part of the rotation curve and  $l_{\text{flat}}$  describes the radius at which the rotation velocity flattens.

The H I radius,  $R_{\text{HI}}$ , is measured from the H I column density profiles.  $R_{\text{HI}}$  is defined to be the radius at which the H I column density drops to  $1 M_{\odot} \text{pc}^{-2}$ . Before  $R_{\text{HI}}$  is measured, H I column densities are deprojected by multiplying with the cosine of the inclination  $\cos i$ . Therefore, in more edge-on galaxies, the measurement of  $R_{\text{HI}}$  is more sensitive to inclination variations than in more face-on galaxies. The radius is determined by linearly extrapolating the two column density profile data points just above and just below  $1 M_{\odot} \text{pc}^{-2}$ . Following Wang et al. (2014, 2016),  $R_{\text{HI}}$  is then corrected for beam smearing effects. This reduces  $R_{\text{HI}}$  on average by 1 per cent and at most by 4 per cent

The combination of the stellar or H I mass profiles with the rotation curve allows one to calculate the stellar or H I specific angular momentum of the disc following

$$j = \frac{\sum_i M_i \times V_{\text{rot},i} \times r_i}{\sum_i M_i} \quad (5)$$

(Obreschkow & Glazebrook 2014; Obreschkow et al. 2016), where  $M_i$  is the mass of ring *i* with radius  $r_i$  rotating at velocity  $V_{\text{rot},i}$ . The baryonic specific angular momentum is the mass-weighted average of the stellar and H I specific angular momenta. Because the angular momentum is a vector, if the velocity vectors of each annulus are not aligned, as is the case for warps, then the amplitude of the total angular momentum is smaller than the sum of the angular momenta in each annuli. We do not correct for this effect in our analysis. The fitted inclination warps are of the order of 10 degrees or less. This would translate into a 2 per cent decrease in angular momentum.

Note, this way to estimate a “stellar” specific angular momentum assumes, that the kinematics of the stellar disc behave as the kinematics of the H I disc. In particular in the centres of galaxies, this is not always the case (Bershady et al. 2010; Cortese et al. 2016, 2014)

The baryonic specific angular momentum ( $j_{\text{B}}$ ), together with the velocity dispersion ( $\sigma$ ), as fitted with TiRiFiC, and the baryonic mass ( $M_{\text{B}}$ ) determine the global stability parameter  $q$  (Obreschkow et al. 2016):

$$q = \frac{j_{\text{B}} \cdot \sigma}{G \cdot M_{\text{B}}} \quad (6)$$

( $G$  is the gravitational constant). The values measured as described in this section will be used to analyse the HIX galaxies in the next section.

When attempting to estimate the dark-matter halo spin parameter for real galaxies, we have to make some assumptions. Here we use equ. (19) of Obreschkow & Glazebrook (2014) and follow their suggested values for the ratio of cold baryon mass (i. e. the sum of the stellar, H I and H<sub>2</sub> masses) to halo mass ( $f_{\text{M}} = 0.05$ ) and ratio of the specific angular momentum of cold baryons to that of the halo ( $f_j = 1$ ), based on the results of Stewart et al. (2013), McMillan (2011), Flynn et al. (2006), Kalberla & Dedes (2008), and Sanders et al.

ID	$V_{\text{rot}}$ [km s <sup>-1</sup> ]	$R_{25}$ [kpc]	$PA_0$ [deg]	$INCL_0$ [deg]	$\Delta PA$ [deg]	$\Delta INCL$ [deg]
(1)	(2)	(3)	(4)	(5)	(6)	(7)
ESO111-G014	204.4	23.5	337.9	55.6	12.4	15.9
ESO243-G002	166.5	16.4	349.9	47.7	0.0	0.0
NGC0289	191.0	11.0	135.6	48.2	18.6	24.1
ESO245-G010	192.4	23.5	25.5	72.8	7.5	8.3
ESO417-G018	173.9	19.9	357.0	57.8	3.0	5.1
ESO055-G013	196.8	8.1	51.1	26.4	48.2	3.2
ESO208-G026	143.1	6.6	286.0	63.1	16.9	34.1
ESO378-G003	134.8	10.3	354.8	62.7	15.2	4.7
ESO381-G005	122.4	11.7	313.4	55.3	85.3	8.5
ESO461-G010	153.9	17.3	77.4	83.9	21.8	5.5
ESO075-G006	217.5	21.0	315.9	39.8	35.6	5.3
ESO290-G035	181.6	23.7	338.2	81.5	21.3	1.8
NGC 685	127.7	9.1	100.3	36.0	0.0	0.0
ESO121-G026	200.7	11.8	294.4	44.9	0.0	0.0
ESO123-G023	157.8	12.8	288.8	90.0	22.0	31.1
NGC 3001	249.6	14.3	185.4	51.1	16.0	3.0
ESO263-G015	159.3	14.7	289.2	90.0	3.0	9.7
NGC 3261	349.4	17.3	256.7	42.3	37.9	9.9
NGC 5161	175.0	19.6	250.7	63.3	13.0	15.9
ESO383-G005	207.0	22.7	310.3	85.3	11.7	3.4
IC 4857	154.6	17.1	33.8	53.5	28.4	19.0
ESO287-G013	175.5	19.0	241.4	81.0	0.0	0.0
ESO240-G011	266.0	31.6	127.1	87.0	0.0	0.0

**Table 3.** Results of the TiRiFiC modelling. The final models of galaxies marked with \* are FLAT models, all other galaxies are modelled with WARP models. *Column* (1): The galaxy ID. *Column* (2): The rotation velocity in  $km\ s^{-1}$ . *Column* (3): the  $B_J$ -band 25 mag arcsec<sup>-2</sup> isophotal radius in kpc. *Columns* (4) and (5): the position angle and inclination values fitted to the rings inside of  $R_{25}$ . *Columns* (6) and (7): the difference between the largest and the smallest position angle and inclination values respectively.

(1984). This leads to the following equation:

$$\lambda = \left[ \frac{M_B [M_\odot]}{10^{10}} \right]^{-2/3} \times \frac{j_B [\text{kpc km s}^{-1}]}{10^3} \times 0.069 \quad (7)$$

Note, however, that in practice, there is a large scatter in the quantities that are used in this calculation (Romanowsky & Fall 2012; Obreschkow & Glazebrook 2014; Stevens et al. 2016; Lagos et al. 2017a).

## 2.6 Data for comparison with HighMass galaxies

We will compare the specific angular momentum and halo spin properties of HIX galaxies to four HighMass galaxies (Huang et al. 2014), for which resolved H I maps and accurately measured halo spin parameter are published (Hallenbeck et al. 2014, 2016). The measurements for these galaxies are summarised in Tab. 5. The stellar mass of these galaxies has been calculated from  $K$ -band photometry the same way as for HIX galaxies (see Equ. 1). The baryonic mass is calculated from stellar and H I mass as detailed in Equ. 3. The baryonic specific angular momentum has been calculated from the halo spin parameter using Equ. 7. The stability parameter is then determined as for the HIX galaxies (see Equ. 6), assuming a velocity dispersion of  $\sigma = 11\text{ km s}^{-1}$ .

There has been a fifth HighMass galaxy (NGC 5230) for which resolved H I maps have been published, however, due to its low inclination, Hallenbeck et al. (2016) refrain from measuring a spin parameter in this galaxy.

## 3 RESULTS

### 3.1 Masses and sizes

As detailed in Lutz et al. (2017), the HIX galaxy sample was selected to contain more H I than expected from their stellar luminosity using scaling relations by Dénes et al. (2014). This translates into HIX galaxies containing a high H I to stellar mass fraction for their stellar mass. Fig. 1 shows that this is the case for most HIX galaxies. So far we have found that the stellar discs of the HIX galaxies are similar to those of the control sample in terms of star formation activity and morphology. This means that the extreme H I content of HIX galaxies does not drive extreme star formation.

We now investigate a stellar mass–size relation. The relation between stellar mass and the  $K$ -band effective radius is shown in Fig. 2. As stellar masses are calculated from  $K$ -band luminosities, radii in the  $K$ -band are treated as equivalent to stellar radii. For the galaxies in the HIPASS parent sample that are identified with a 2MASX counterpart, a correlation between  $M_*$  and  $R_*$  is seen. This relation is in good agreement with the corresponding scaling relation for GAMA galaxies (Lange et al. 2015). Both the HIX and the control sample follow this relation. Thus in terms of average stellar surface density, the stellar discs of HIX galaxies are similar to the stellar disc of the control sample.

Fig. 3 shows the relation between the H I disc size and H I mass for the HIX and the control sample. Both samples follow the Wang et al. (2016) relation, which was fitted to around 400 galaxies and is in good agreement with the previous relation by Broeils & Rhee (1997). All HIX and control galaxies have average H I column densities and their H I discs behave as average H I discs in the local Universe.

ID	RA DEC	D Mpc	$\log M_*$ [ $M_\odot$ ]	$\log M_{\text{HI,HIP}}$ [ $M_\odot$ ]	$\log M_{\text{HI,ATCA}}$ [ $M_\odot$ ]	$R_{\text{HI}}$ [kpc]	$R_{\text{eff}}$ [kpc]	$j_B$ [kpc km s $^{-1}$ ]	$\lambda$	$\log q$
(1)	(2)	(3)	(4)	(5)	(6)	(7)	(8)	(9)	(10)	(11)
ESO111-G014	00:08:18.8 -59:30:56	111.98	10.5	10.7	10.6	49.6	6.0	4125.6	0.06	-0.84
ESO243-G002	00:49:34.5 -46:52:28	128.87	10.7	10.8	10.7	55.6	7.2	3523.8	0.05	-0.82
NGC 289	00:52:42.4 -31:12:21	23.06	10.5	10.4	10.5	86.9	2.9	5453.1	0.10	-0.59
ESO245-G010	01:56:44.5 -43:58:21	81.69	10.5	10.3	10.5	50.9	6.2	4092.4	0.07	-0.63
ESO417-G018	03:07:13.2 -31:24:03	67.35	10.3	10.6	10.4	45.5	5.7	3522.7	0.08	-0.74
ESO055-G013	04:11:43.0 -70:13:59	104.98	10.2	10.5	10.3	41.0	2.3	3749.8	0.10	-0.68
ESO208-G026	07:35:21.1 -50:02:35	39.72	9.8	9.8	9.9	28.8	1.8	1993.0	0.10	-0.45
ESO378-G003	11:28:04.0 -36:32:34	40.56	10.1	10.3	10.3	44.3	4.8	3196.7	0.09	-0.51
ESO381-G005	12:40:32.7 -36:58:05	80.04	10.1	10.4	10.4	37.8	3.3	3388.2	0.08	-0.47
ESO461-G010	19:54:04.4 -30:29:03	98.26	10.1	10.7	10.3	23.7	4.0	6377.8	0.17	-0.31
ESO075-G006	21:23:29.5 -69:41:05	153.94	10.6	10.8	10.9	94.0	3.8	9764.0	0.11	-0.76
ESO290-G035	23:01:32.5 -46:38:47	84.50	10.5	10.4	10.5	36.3	5.3	4117.7	0.08	-0.74
NGC 685	01:47:42.8 -52:45:42	17.97	9.8	9.6	9.6	16.1	5.4	821.0	0.05	-0.70
ESO121-G026	06:21:38.8 -59:44:24	29.64	10.3	10.0	9.6	21.5	3.4	1041.3	0.04	-1.14
ESO123-G023	07:44:38.9 -58:09:13	38.63	10.0	9.9	10.0	30.0	3.7	2193.1	0.09	-0.59
NGC 3001	09:46:18.7 -30:26:15	32.14	10.7	10.0	9.8	30.9	3.9	1469.1	0.03	-1.21
ESO263-G015	10:12:19.9 -47:17:42	33.13	10.3	9.6	9.8	22.5	5.9	2447.9	0.08	-0.72
NGC 3261	10:29:01.5 -44:39:24	33.59	10.8	10.2	10.0	30.8	4.5	2252.0	0.04	-1.14
NGC 5161	13:29:13.9 -33:10:26	32.23	10.6	10.3	10.3	41.6	6.0	2294.8	0.05	-0.91
ESO383-G005	13:29:23.6 -34:16:17	50.20	10.6	9.7	9.7	23.8	4.1	2035.6	0.05	-1.01
IC 4857	19:28:39.2 -58:46:04	66.50	10.5	10.5	10.0	35.1	7.9	2095.4	0.05	-0.78
ESO287-G013	21:23:13.9 -45:46:23	38.72	10.5	10.2	10.2	38.3	4.4	4095.8	0.07	-0.86
ESO240-G011	23:37:49.9 -47:43:41	40.12	10.8	10.5	9.8	29.2	5.7	1907.1	0.05	-0.92

**Table 4.** Basic properties and measurements for the HIX (above the horizontal line) and control galaxy sample (below the horizontal line). *Column (1)*: Galaxy ID. *Column (2)*: 2MASX coordinates of the stellar centre. *Column (3)*: distance in Mpc. *Column (4)*: Stellar masses as calculated from the 2MASX *K*-band luminosity. *Column (5)*: H I mass as measured from HIPASS data cubes. *Column (6)*: H I mass as measured from ATCA data cubes in this work. *Column (7)*: The H I radius as measured at the  $1 M_\odot \text{pc}^{-2}$  isophote in kpc. *Column (8)*: The 2MASX *K*-band half-light radius in kpc. *Column (9)*: The baryonic specific angular momentum in units of [kpc km s $^{-1}$ ]. *Column (10)*: The halo spin parameter inferred from the baryonic specific angular momentum. *Column (11)*: The global stability parameter  $q$ .

	UGC 9037	UGC 12506	UGC 6168	UGC 7899
$\lambda^*$	0.07	0.15	0.09	0.08
$\log M_{\text{HI}} [M_\odot]^*$	10.33	10.53	10.35	10.42
$\log M_* [M_\odot]$	10.45	10.79	10.43	10.82
$\log M_B [M_\odot]$	10.75	11.03	10.76	11.01
$j_B$ [kpc km s $^{-1}$ ]	3239	10583	4169	5438
$\log q$	-0.84	-0.60	-0.73	-0.86

**Table 5.** Properties for four HighMass galaxies. Properties marked with \* are taken from Hallenbeck et al. (2014, 2016). All other properties are calculated as described in the text.

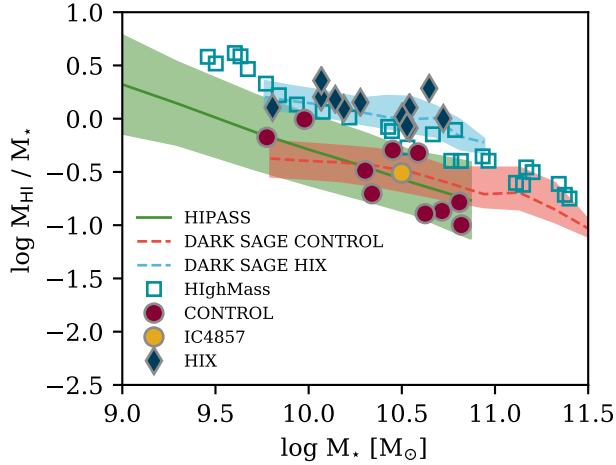


**Figure 1.** The H I-to-stellar mass ratio as a function of the stellar mass. The green shaded area shows the  $1\sigma$  range of the parent sample (with 2MASS cross match), red circles give the control sample and blue diamonds represent the HIX sample. The yellow circle is IC 4857, which was initially selected as a HIX galaxy, but then reclassified to a control galaxy. The empty blue squares present the HighMass sample. Orange and light blue dashed lines indicate the running average of simulated HIX (light blue) and control galaxies (orange) from the DARK SAGE semi-analytic model (for more details see Sec. 4). The orange and light blue shading covers the 16 to 84 percentile range. As per sample selection, HIX galaxies have high H I mass fractions for their stellar mass.

Both the H I and the stellar discs of the HIX and control samples fall on the same respective mass-size relations. However, the HIX galaxies have more massive H I discs than the control sample. Therefore, we also compare the  $R_{\text{HI}}$  and the  $K$ -band effective radius in Fig. 4. As expected, the H I-to-stellar disc size ratio is larger for most HIX galaxies. Exceptions are two HIX galaxies, for which the data points are located within the scatter of the control sample data. These two galaxies are ESO461-G010 and ESO290-G035.

ESO461-G010 and ESO290-G035 are the two only HIX galaxies with TiRiFiC inclination angles above  $80^\circ$ . This might hamper the measurements. There are also four control galaxies with such high inclinations, these galaxies are however at smaller distances and thus better resolved.

The two galaxies with the largest H I to stellar diameter ratios and H I diameters above 150 kpc are NGC 289 and ESO075-G006. The “smaller” of the two galaxies is NGC 289. This galaxy has been studied extensively before. (Walsh et al. 1997) has classified NGC 289 as a low surface brightness galaxy with a high surface brightness inner disc. Latest photometry shows a central surface brightness in  $R$ -band of  $\sim 17 \text{ mag arcsec}^{-2}$  (Li et al. 2011), i. e. the central disc is a high surface brightness disc<sup>3</sup>. In addition, NGC 289 has been found to host an extended UV disc (XUV disc) and has star forming regions beyond the optical disc (Meurer 2017). There is a potential dwarf galaxy, PGC 708504, which is not detected by 2MASS and is not detected as a separate H I source in our ATCA data. In particular in that respect

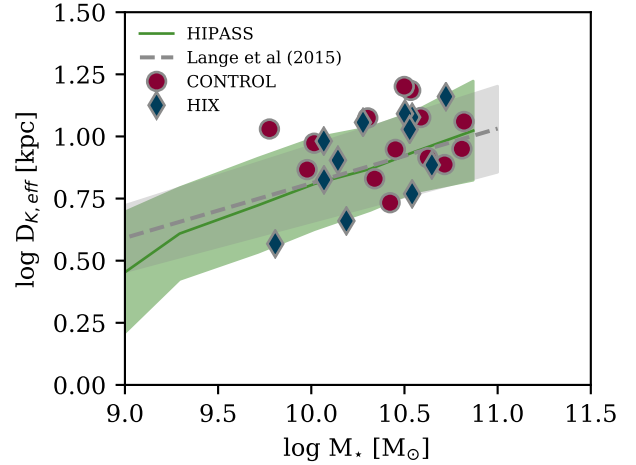


**Figure 2.** A stellar mass-size relation. The running average of the HIPASS parent sample is shown as the solid, green line, with the  $\pm 1\sigma$  scatter as the green shaded area. For comparison the grey dashed line and grey shaded area give the mass-size relation and its errors for late-type galaxies from the GAMA survey (Lange et al. 2015). The control and HIX sample galaxies are shown as red circles and blue diamonds respectively. The HIX and control sample galaxies occupy a similar parameter space and follow the relation from the literature and the parent sample.

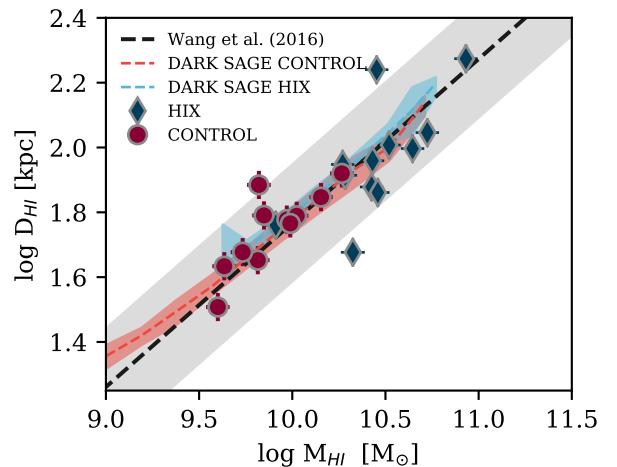


**Figure 3.** The relation between H I disc size and mass. Blue diamonds present the HIX sample and red circles the control sample. The grey dashed line is the relation found by Broeils & Rhee (1997), confirmed by Wang et al. (2016), where the grey shaded area covers their  $3\sigma$  scatter of 0.18 dex. As in Fig. 1 light blue and orange dashed lines present DARK SAGE simulated galaxies and the shaded areas their respective 16 to 84 percentile ranges. H I masses and sizes of the HIX galaxies are consistent with the literature relation.

NGC 289 is remarkably similar to ESO075-G006, which also has a nearby dwarf companion without an H I detection (for a more detailed discussion see Lutz et al. 2017). The *GALEX* *NUV* image of ESO075-G006 has a much shorter exposure time than the one of NGC 289 (207 s compared to 1696 sec) and optical imaging is of lower quality. Hence, a XUV disc or an extend low surface brightness stellar disc can not be included in ESO075-G006. However, given the large H I col-

<sup>3</sup> for detailed photometric profiles see <https://cgs.obs.carnegiescience.edu/CGS/object.html#pages/NGC289.html>



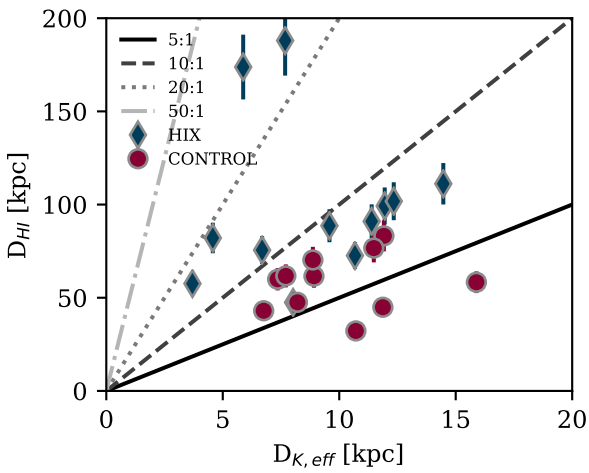


**Figure 4.** The relation between  $R_{\text{HI}}$  and the  $K$ -band effective radius. Blue diamonds present the HIX sample and red circles the control sample. Grey lines denote different ratios between the two sizes. At a given  $K$ -band effective radius, HIX galaxies tend to have larger H I disc sizes than the control sample.

umn densities above  $1 M_{\odot} \text{pc}^{-2}$  well outside the visible disc of ESO075-G006, star formation in an XUV disc is also a possibility in this galaxy. If this is the case, then galaxies with very large H I to stellar disc sizes might be galaxies with a high surface brightness inner disc and an extended low surface brightness outer disc.

Interestingly, the H I disc of ESO208-G026 is approximately 7.5 times larger than the stellar disc, despite the fact that this galaxy is located less than  $1\sigma$  above the running average of HIPASS in Fig. 1. In the H I mass–size plane, this galaxy lies right on the Wang et al. (2016) relation. In the stellar mass–size plane, this galaxy is located approximately  $1\sigma$  below the running average of HIPASS. ESO208-G026 has been classified as S0 by the RC.3 catalogue (de Vaucouleurs et al. 1991) and upon inspection of optical images, a bright bulge and a very faint disc can be seen (see App. A). Therefore the effective radius is small. There is a second S0 galaxy in the HIX sample: ESO055-G013. This galaxy has a gas mass fraction more than  $1\sigma$  above the HIPASS running average. In terms of stellar and H I radii it still behaves similar to ESO208-G026.

### 3.2 Warps and tails in H I discs

In this section we compare the grade of lopsidedness, warps and tails in the H I discs of the control and HIX galaxies. We use the results from the TiRiFiC modelling and visually inspect the moment maps of both samples.

One out of twelve HIX (8 percent) and three out of eleven control galaxies (27 percent) are well fitted with a FLAT disc model. The remaining galaxies are fitted with a WARP model. Hence, a higher percentage of control than HIX galaxies can be described as flat discs.

If a disc is fitted as a warped disc, the range of the inclination is of the same magnitude in both the HIX and the control galaxies. The span of the position angles in one fit tends to be larger in HIX than control galaxies. This trend is mostly driven by HIX galaxies ESO208-G026, ESO378-

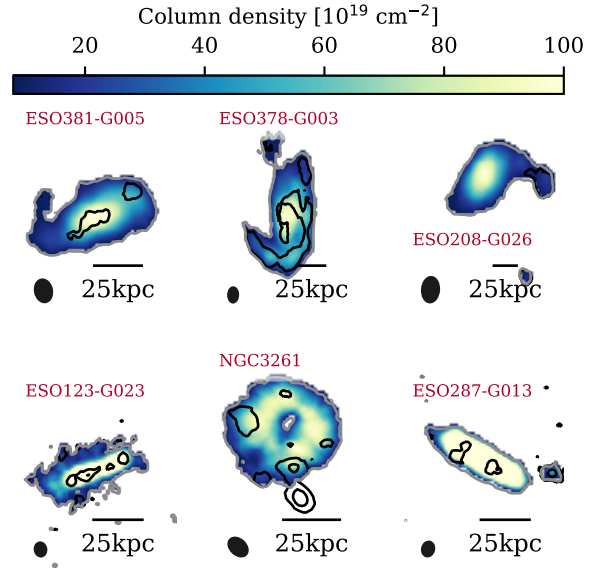


**Figure 5.** Examples for H I moment 0 maps for HIX (top row, from left to right: ESO208-G026, ESO378-G003 and ESO381-G005) and control galaxies (bottom row, from left to right: ESO123-G023, NGC3261 and ESO287-G013). The colour scale indicate H I column densities of the measured data, in the range from  $8$  to  $100 \times 10^{19} \text{cm}^{-2}$ . The grey contour shows the lower limit of the colour scale at  $8 \times 10^{19} \text{cm}^{-2}$ . The overlaid black contours indicate structures in residual moment 0 maps also at column densities of  $8 \times 10^{19} \text{cm}^{-2}$ . Red crosses mark locations of nearby dwarfs or potential stellar debris from minor mergers. The images are 3.6 arcmin in size, except for the image of ESO378-G003, which is 6 arcmin in size. [Figure or Table updated]

G003 and ESO381-G005. These galaxies host prominent arm features (see Fig. 5 and App. A), which TiRiFiC models with a large warp in position angle. We will further discuss these three galaxies below.

The thickness of the disc is also modelled in TiRiFiC. However, the disc thickness is not resolved in most cases. This means that measurements of disc thickness can only be upper limits. Within these limitations, HIX galaxy models have thicker discs than control galaxies. However, when comparing the ratio between disc thickness and disc size, both samples are again more similar, with the ratio being around 5 to 10 percent in most cases. The ratio between disc size and thickness is more meaningful to decide between thick and thin disc because at a given absolute disc thickness only this ratio can inform whether a thin disc or a spheroid is at hand. Outliers with larger ratios are HIX galaxies ESO243-G002, ESO055-G013 and ESO075-G006. Following the Galactic Fountain model, thick discs might indicate active gas accretion in these galaxies. However, these three galaxies are among the four galaxies farthest away. Thus, their disc thickness might be most overestimated by beam smearing.

As mentioned above, galaxies ESO208-G026, ESO378-G003 and ESO381-G005 are fitted with the strongest warps. Upon visual inspection, these galaxies also show the most interesting H I morphologies with H I tails, arms and clouds. Images in the top panel of Fig. 5 show the moment 0 maps of these galaxies. To further quantify the contribution of these

peculiar morphologies to H I-richness, we generate (not fit) flat disc model data cubes for all galaxies with TiRiFiC. These cubes are generated with the following parameters:

- the previously fitted TiRiFiC column density profile,
- the fitted rotation curve (functional form as in Equ. 4),
- radially constant position angle and inclination (the median of the warped profiles),
- velocity dispersion, systemic velocity and kinematic centre as found previously with the fully fitted TiRiFiC model.

For galaxies with a FLAT TiRiFiC fit, these generated cubes are the same as the fitted model cube. For galaxies with a warped TiRiFiC fit, these generated data cubes are “rectified” versions of the fitted model cube.

In a next step we subtract the generated cube from the observed data cube. If the moment 0 map of this residual cube shows structure, the H I mass is measured. This is the case for  $(42 \pm 19)$  and  $(36 \pm 18)$  per cent of the HIX and the control galaxies, respectively. Hence, within Poisson errors, residual structures are found in the same percentage of HIX galaxies as control galaxies. Fig. 5 shows examples for HIX (top row) and control galaxies (bottom row) with residual structures (black contours).

For those galaxies with residual structure, the average fraction of residual H I to total H I mass is  $\text{change}(19 \pm 6)$  and  $(9 \pm 8)$  per cent for HIX and control galaxies. Hence, HIX galaxies tend to host more H I that does not agree with a flat, regularly rotating disc than control galaxies. It has to be noted though that the residuals of the full model data cubes are of the same order. However, according to this measurement, the irregular H I can not fully account for the higher than expected H I mass in HIX galaxies. So irregular gas is not the sole driver of H I excess in HIX galaxies. In addition some of the irregular gas in control galaxies might be missed due to the less sensitive observations.

The reason for the irregularity of the HIX galaxies in Fig. 5 can only be speculated about: ESO208-G026 is located in a relatively sparse environment. Hence, it would be more likely for the arm to be caused by a gas-rich minor merger than by tidal interaction. However, the stellar disc of ESO208-G026 appears regular and no debris of the merger is found in optical images.

ESO378-G003 is part of the NGC 3783 group (Kilborn et al. 2006) and the elliptical galaxy NGC 3706 is located  $22 \text{ arcmin} = 255 \text{ kpc}$  away (projected distance). Furthermore, Kilborn et al. (2006) has found an isolated H I cloud (GEMS\_N3783\_2) without apparent optical counterpart (see their fig. 6 for a resolved map). They concluded the cloud to be a remnant of tidal interaction. This tidal interaction could have potentially disturbed the H I distribution of ESO378-G003 as well.

In ESO381-G005 the arm feature is aligned with wide spiral arms and points towards a dwarf companion (PGC 629239) towards the south, which is also detected in H I. Additionally the inspection of optical images reveals three more sources aligned within the arm that are not foreground stars (PGC630365, USNO A2 0525-15319577 and USNO A2 0525-15322378), but look more like potential debris. Their position on the H I column density map is marked with black crosses in Fig. 5. This might indicate a recent minor merger. However, in order for the minor merger to in-

crease the H I content of a galaxy from control sample levels to HIX sample levels, it would have had to bring in almost  $10^{10} M_{\odot}$  without changing the stellar disc a lot. This appears very unlikely to be the only cause why ESO381-G005 is a HIX galaxy.

In summary, both the HIX and control galaxies show warped discs. HIX galaxies tend to be fitted with stronger warps and are more likely than the control galaxies to have tails or ill-defined outskirts. As mentioned before, the differences in sensitivity of the observations might increase the difference in H I morphology between HIX and control galaxies. Homogeneous, large surveys of the resolved H I content of galaxies, such as the Wallaby survey, will help to shed more light onto this problem. Even in the most irregular HIX galaxies, the amount of H I in arms and tails appears not to be sufficient to explain why these galaxies host more than 2.5 times more H I than expected.

### 3.3 Global stability parameter $q$

So far the analysis has shown that the most striking difference between HIX and control sample is the difference in the H I disc mass and subsequently size. It has long been known that the galaxy size is determined by the angular momentum of the galaxy (Fall & Efstathiou 1980; Dalcanton et al. 1997; Mo et al. 1998). More recently, Maddox et al. (2015) and Obreschkow et al. (2016) have suggested based on ALFALFA (Giovannelli et al. 2005) and THINGS data (Walter et al. 2008) that the H I mass (and thus size), and atomic-to-baryonic mass fraction is regulated by the angular momentum properties of the galaxy. Huang et al. (2014) and Hallenbeck et al. (2014) suggest that the H I-rich galaxies in the HighMass sample are H I-rich due to an increased specific angular momentum. A higher specific angular momentum affects the disc in two ways:

- (i) Gas is stabilised against gravitational collapse and subsequent star formation.
- (ii) H I is kept at larger galactocentric radii, where the total disc density is too low to form molecular hydrogen and stars.

Thus, a galaxy with a higher specific angular momentum can support a larger H I disc. This stability can be quantified as the global stability parameter  $q$  (Obreschkow et al. 2016, see also Sec. 2.5), which is proportional to a disc wide average of the local Toomre  $Q$  parameter (Toomre 1964). A more descriptive way to understand and interpret this parameter is the following: Consider the radial variation of the Toomre  $Q$  parameter in two galaxies with a similar exponential discs (i.e. similar scale radii) but different  $q$ 's. In the galaxy with the larger  $q$ , H I begins to be Toomre-stable at smaller radii than in the galaxy with a smaller  $q$  (see fig. 1 in Obreschkow et al. 2016).

Fig. 6 shows the atomic-to-baryonic mass fraction as a function of  $q$ . Most of the HIX and the control sample follow this model within the scatter of the analytical model of Obreschkow et al. (2016). This means that galaxies from both samples host as much H I as they can support against star formation. For comparison, we also show THINGS galaxies (data taken from Obreschkow & Glazebrook 2014) and HighMass galaxies (Huang et al. 2014; Hal-

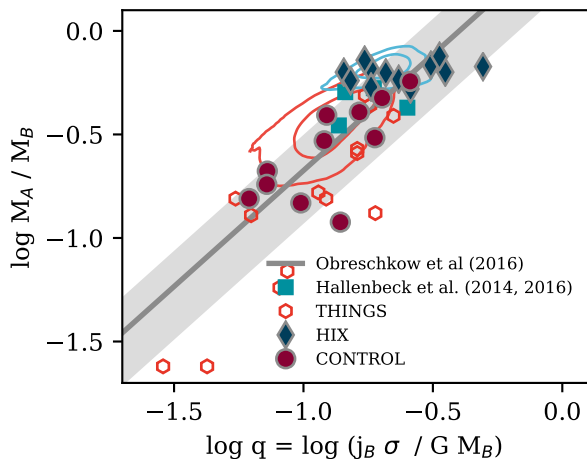


**Figure 6.** The atomic to baryonic gas ratio as a function of the global stability parameter. In addition to the data of the HIX (blue diamonds) and control sample (red circles), we also show data of THINGS galaxies (orange pentagons, Obreschcow & Glazebrook 2014) and HighMass galaxies (light blue squares). The orange and light blue contours encompass 68 and 95 per cent of the simulated control and HIX galaxies from DARK SAGE (for more details see Sec. 4). The data of observed and simulated galaxies agree with the analytical model of Obreschcow et al. (2016).

lenbeck et al. 2014, 2016) (see Sec. 2.6 for more details on the data). Both samples also follow the model.

Most HIX galaxies have systematically larger global stability  $q$  values than the control galaxies. This is due to a larger baryonic specific angular momentum, which is driven by a larger HI specific angular momentum. Rotation velocities are of similar magnitude in HIX and control galaxies (see Tab. 4). So the large HI specific angular momenta in HIX galaxies are mostly due to large masses of high angular momentum gas located at large galactocentric radii.

The question now is: why do HIX galaxies have high specific HI angular momenta. In the cases of galaxies, ESO378-G003, ESO381-G003 and ESO208-G026, which were discussed in the previous section, the gas might have been recently accreted or dislocated in some interaction. Other galaxies might be living in high-spin haloes, which gives them an intrinsically high specific angular momentum. To test this hypothesis, we compare our galaxies to simulated galaxies from the semi-analytic model DARK SAGE in the next section.

#### 4 COMPARISON WITH DARK SAGE

We use the semi-analytic model DARK SAGE (Stevens, Croton & Mutch 2016) to investigate how the dark-matter halo spin affects the HI content of HIX galaxies. Semi-analytic models use halo merger trees, typically produced from a cosmological  $N$ -body simulation, as input for a series of coupled differential equations that describe the evolution of galaxies (see reviews by Baugh 2006; Somerville & Davé 2015). DARK SAGE is an ideal model for our investigation, as, other than when a galaxy is first initialised in the model, there are no assumptions made about the relationship between the instantaneous spin of a (sub)halo and the galaxy it hosts (see

Stevens et al. 2017 and references therein for a discussion on the importance of this). Instead, a galaxy’s specific angular momentum depends on the entire history of its halo’s spin evolution, along with its merger history, and its own secular evolution. Furthermore, in addition to other properties, the model is calibrated to the observed HI mass function (Zwaan et al. 2005) and to the mean HI-to-stellar mass fraction of galaxies as a function of stellar mass (Brown et al. 2015).

The unitless spin parameter of a dark-matter halo is defined as

$$\lambda \equiv \frac{J|E|^{1/2}}{GM_{\text{vir}}^{5/2}} = \frac{j_{\text{halo}}}{\sqrt{2}R_{\text{vir}}V_{\text{vir}}} \quad (8)$$

(Peebles 1969; Bullock et al. 2001), where  $J$  is the halo’s total angular momentum,  $E$  its total energy,  $M_{\text{vir}}$  its virial mass,  $j_{\text{halo}}$  its specific angular momentum,  $V_{\text{vir}}$  its virial velocity, and  $R_{\text{vir}}$  its virial radius. Simulations show that the spin parameters of haloes follow an approximately log-normal distribution with a peak around 0.03 (Barnes & Efstathiou 1987; Bullock et al. 2001; Shaw et al. 2006).

At each time-step in DARK SAGE, gas can cool onto a galaxy from its halo. The net specific angular momentum of the gas that cools is assumed to be the same as that of halo at that instant (related to  $\lambda$  through equ. 8). This gas is distributed with an exponential profile into 30 disc annuli, each of which has a fixed specific angular momentum. The angular momentum vector of this gas is then summed with that already in the galaxy to define the gas disc’s new plane, and both distributions are projected onto a new set of annuli in that plane. Frequent changes to the halo’s spin direction (or magnitude) and mergers can lead to a reduction in the galaxy’s specific angular momentum. Full details are provided in Stevens et al. (2016).

#### 4.1 The simulated galaxy catalogue

We obtain a box-type catalogue of simulated galaxies from the Theoretical Astrophysical Observatory (TAO<sup>4</sup>, Bernyk et al. 2016). The underlying dark-matter-only simulation is the Millennium simulation (Springel et al. 2005). We use the full box size of  $(500\text{Mpc}/h)^3$  and consider the snapshot at  $z=0$ . The Millennium simulation uses the cosmological parameters from WMAP-1 (Spergel et al. 2003). Note, however, that we apply  $H_0 = 70\text{ km Mpc}^{-1}\text{ s}^{-1}$  where relevant to these data to be consistent with the presentation of our observational data. The dark-matter haloes are populated using the 2016 version of the DARK SAGE semi-analytic model (Stevens et al. 2016). Because DARK SAGE evolves galaxy discs in annuli of constant specific angular momentum, the model can make predictions on structural and kinematic properties of the simulated galaxies.

In addition to the galaxy parameters that DARK SAGE computes, TAO can also fit the spectral energy distribution (SED) of a galaxy and thus calculate its brightness in given filters. In our case, we chose Bruzual & Charlot (2003) SEDs with a Chabrier (2003) initial mass function (foreground dust modelling was not included). The final catalogue of simulated galaxies includes masses and angular momenta

<sup>4</sup> <https://tao.asvo.org.au>

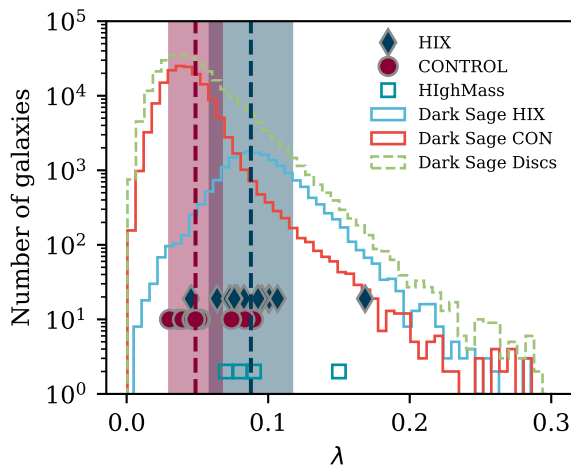


**Figure 7.** Distributions of the halo spin parameter for the DARK SAGE model galaxies (which come directly from Millennium data). The entire disc sample is shown in the green dashed histogram, HIX-like galaxies in the light blue and control-like in the orange histogram. Estimates for the halo spin of single HIX and control galaxies are shown in blue diamonds and red circles and the sample medians are marked with the vertical blue and red dashed line, respectively. The  $1\sigma$  range of the HIX and control galaxies is shaded in the respective colours. For comparison, the spin parameters for four HighMass galaxies as taken from [Hallenbeck et al. \(2014, 2016\)](#) are given as light blue squares. HIX galaxies tend to live in haloes with larger spins.

for each of stars, H I and molecular gas, as well as bulge-to-total mass ratios, H I and stellar disc sizes, absolute  $R$ -band magnitudes, and dark-matter halo spin parameters.

#### 4.2 Selecting DARK SAGE HIX and control galaxies

The HIX and control sample were selected using the  $R$ -band – H I mass scaling relation by [Dénes et al. \(2014\)](#). We use the same relation to select simulated HIX and control galaxies from the DARK SAGE catalogue. We furthermore add a stellar mass cut of  $9.7 \leq \log M_{\text{HI}} [M_{\odot}] \leq 11.2$  and a bulge to total mass ratio cut  $B/T < 0.3$  to select only disc galaxies.

This results in a catalogue of 288385 galaxies of which 18416 (6 per cent) are HIX and 154730 (53 per cent) control sample-like. On the gas mass fraction – stellar mass relation, the H I mass–size relation, and the atomic-to-baryonic mass fraction vs. stability parameter plane the simulated and real samples behave similarly (see their running averages in Figs. 1 and 3 and their contours in Fig. 6).

#### 4.3 Properties of simulated HIX and control galaxies

In Fig. 7 the dark-matter halo spin distribution of the entire DARK SAGE disc sample, the HIX, and control-like DARK SAGE galaxies are shown. The peak of the halo spin distribution of the HIX-like DARK SAGE galaxies is at much higher values than for the control-like galaxies, which agree with the entire DARK SAGE sample.

The estimates for the halo spin of the observed HIX and

control galaxies show a similar albeit weaker trend: the median estimated halo spin (dashed line) is larger for HIX than control galaxies. The galaxy with the largest spin parameter ( $\lambda = 0.17$ ) in the two samples is a HIX galaxy: ESO461-G010.

The control galaxy with the highest spin parameter is ESO123-G023 with  $\lambda = 0.09$ . The spin parameters of 8 out of 11 control galaxies are lower than the spin parameters of 11 (out of 12) HIX galaxies. Only HIX galaxy ESO243-G002 has  $\lambda = 0.05$ .

The four HighMass galaxies that are shown in Fig. 7, are those HighMass galaxies with published resolved H I maps. For the fifth HighMass galaxy with a published resolved H I map no spin parameter has been published. The HighMass galaxies show mostly spin parameters of the same order as the HIX galaxies, except for galaxy UGC 12506 ([Hallenbeck et al. 2014](#)), which lives in a very high-spin halo. This further adds to the evidence from [Lutz et al. \(2017\)](#) that HighMass galaxies are similar to HIX galaxies.

In summary, we were able to select model galaxies from DARK SAGE, that behave similar to our observed HIX and control galaxies. When looking at the halo spin parameters of the modelled galaxies, HIX-like galaxies tend to live in higher spin haloes than control-like galaxies. The estimates of the halo spin parameter in our observed HIX and control galaxies show a similar trend.

## 5 DISCUSSION

HIX galaxies are more likely to host warped discs and/or arms and tails than control galaxies. Fewer HIX galaxies can be described with a flat disc. Some diffuse gas in the control galaxies might be missed due to less sensitive observations. Hence fewer warps might be fitted to the data of control galaxies. Still, the majority of both the HIX and the control galaxies show warps. The cause of warps is not yet fully understood. They can be for example be created in hydrodynamical, cosmological simulations when the angular momenta of the inner disc and of the surrounding halo or accreted gas are misaligned ([Roškar et al. 2010](#)). Hence, the detection of warps in both samples can indicate cold gas accretion. Warps can also be formed by minor mergers ([Sancisi et al. 2008](#)). Many of our sample galaxies have dwarf galaxies nearby, some of which are also detected in H I. If gas-rich, minor mergers can not only cause warps, but can also contribute to the H I content of the galaxy. Furthermore, especially the HIX H I discs reach far into the halo. There they might be more susceptible to interactions with sub-haloes or torques by a mis-aligned outer halo and less supported by the stellar disc. These effects can also lead to warps ([Józsa 2007](#)).

There is one HIX galaxy that shows clear signs of interaction both in its stellar and H I disc (ESO245-G010), and three HIX galaxies that have some kind of H I arms or clouds attached to their disc (ESO208-G026, ESO378-G003 and ESO381-G005). These features might be due to the accretion of gas rich dwarf companions (ESO245-G010 and ESO381-G005) or tidal interaction with another galaxy (ESO378-G003 with NGC 3706). We find, however, that the H I mass of those features is not large enough to fully explain the high H I masses of HIX galaxies. It should be noted that

the kinematic properties of the discs of these galaxies still agree with a model of a marginally stable disc.

There is no control galaxy with any signs of interaction in the stellar disc, but one galaxy hosts irregularly shaped gas at large radii (ESO123-G023). Three control galaxies are accompanied by dwarf galaxies that are detected in our H I data cubes (ESO287-G013, IC4857 and NGC 3261). In summary, HIX galaxies tend to be more lopsided than control galaxies, however, the mass of irregular H I is not high enough to fully explain why they are HIX galaxies.

The environments of the HIX and control galaxies are very diverse. Some galaxies are located just a few Mpc (projected) away from centres of clusters: HIX galaxy ESO243-G002 resides 2.2 Mpc away from ABELL 2836 and control ESO383-G005 galaxy is located 1 Mpc away from ABELL 3563. Other galaxies are very isolated. The nearest neighbour within  $\pm 500 \text{ km s}^{-1}$  in recession velocity for example of ESO208-G026 according to NED<sup>5</sup>, is ESO208-G031 at a projected distance of 1.7 Mpc.

Resolved H I maps have been published for five HighMass galaxies (Hallenbeck et al. 2014, 2016). None of these galaxies show any signs of arms, tails or diffuse and irregular edges to their column density limits of  $> 8.4 \times 10^{20} \text{ cm}^{-2}$ . This limit, however, is about 10 to 20 times higher than our column density limits and thus too high to detect arms as hosted by ESO208-G026, ESO378-G003 and ESO381-G005.

When considered independently, H I and stellar discs of both samples follow the same mass–size relations (Figs. 2 and 3). Hence, the average H I and stellar column densities are as average for a galaxy in the local Universe in both samples.

However, the H I discs of the HIX galaxies extend further beyond the stellar disc than those of control galaxies. HIX galaxies host H I at larger galactocentric radii than control galaxies. This gas has a larger specific angular momentum and can therefore not flow to the central parts of the galaxy. Due to the low overall density (no detected stellar disc component) at these large galactocentric radii, this gas is furthermore unable to collapse and form stars.

The high specific angular momentum of this H I gas at large radii heavily contributes to the total specific baryonic angular momentum, which is higher in HIX than in control galaxies. Evidence points to the specific baryonic angular momentum as a primary regulator of H I disc size and mass. This is in agreement with the Obreschkow et al. (2016) model (Fig. 6) and the results of hydrodynamical simulations (Lagos et al. 2017b).

In HIX galaxies, the high H I specific angular momentum is actually the sole driver of an elevated baryonic specific angular momentum. The stellar specific angular momenta (based on H I kinematics) are of similar size in the HIX and control sample. This observation is reflected in the stellar mass–size relation, where both samples are located in similar areas. This allows parameters like the specific star formation rate (see section 4.2 in Lutz et al. 2017) or the average stellar

surface density (see Fig. 2) to be similar between the two samples.

From the observations it is not possible to determine how these galaxies acquired significant amounts of H I at large radii or why their specific baryonic angular momentum is elevated. In Sec. 4, we have used the semi-analytic galaxy model DARK SAGE built on the dark-matter Millennium simulation. HIX-like galaxies in this simulated galaxy catalogue tend to live in dark-matter haloes with a larger spin than control-like galaxies. The estimated dark-matter spins for HIX galaxies show a similar, but weaker trend: The bulk of the HIX galaxies is within haloes that have higher spin parameters than the bulk of the control galaxies.

So an explanation for most HIX galaxies might be that they are galaxies in intrinsically high-spin haloes. Thus, their high baryonic specific angular momentum is inherited from the halo. The HIX galaxies with a relatively low halo spin are ESO111-G014, ESO243-G002 and ESO245-G010. The ratio of halo to baryonic specific angular momentum is subject to a lot of variation (Übler et al. 2014; Bett et al. 2010). When we estimate the halo spin of the HIX galaxies, we assume a constant halo to baryonic specific angular momentum ration. So on these galaxies, this ratio might have been changed during their history. Simulations suggest some mechanisms that can lead to an increased specific angular momentum (and thus an extended H I disc).

Based on the cosmological, hydrodynamical Illustris simulation, Genel et al. (2015) and Zjupa & Springel (2017) suggest that feedback can tamper with angular momentum in the sense that strong stellar winds increase and AGN feedback decreases the angular momentum of galaxies. Hence, HIX galaxies might have undergone stronger star bursts in the past that removed more low-angular-momentum gas in galactic winds thus increasing the overall specific angular momentum. This is in agreement with cosmological zoom-in simulations by Übler et al. (2014), who find that galaxies simulated with strong stellar feedback have higher angular momenta than galaxies with weak stellar feedback.

Stewart et al. (2011, 2013, 2016) suggest, based on cosmological zoom-in simulations, that gas accreted through cold filamentary accretion increases the angular momentum of the galaxy disc. In particular Stewart et al. (2013) finds that gas accreted in the cold mode forms a so called cold flow disc which corotates with the galaxy disc. They suggest that these cold flow discs might be observed as extended H I or UV disc today. In their picture, HIX galaxies might be galaxies which accreted gas that was never shock heated. Furthermore, the specific angular momentum can be increased in minor and/ or gas-rich mergers (Lagos et al. 2017a).

The HIX galaxies with a relatively low halo spin might, also be galaxies in transition. ESO245-G010 for example shows clear signs of a recent merger. Large gas masses at large radii might move further towards the centre of the galaxy and be used for star formation, once the disc settles.

## 6 SUMMARY AND CONCLUSIONS

In this second paper on the HIX galaxies, we have analysed the spatially resolved H I distribution and kinematics of the HIX and the control galaxies. Our findings can be summarised in the following three points:

<sup>5</sup> <http://ned.ipac.caltech.edu>, The NASA/IPAC Extragalactic Database (NED) is operated by the Jet Propulsion Laboratory, California Institute of Technology, under contract with the National Aeronautics and Space Administration.

(i) The stellar and H I discs of the HIX and control samples follow the same respective mass–size relations. This means that the stellar discs of the HIX galaxies behave like average stellar discs, and the H I discs of HIX galaxies are consistent with average H I discs in the local Universe. Only the relation between H I and stellar disc within HIX galaxies makes them outliers to the Dénes et al. (2014) scaling relations.

(ii) We find the H I discs of galaxies in the HIX sample are more likely to be warped and irregular than in the control sample. Yet, most control galaxies are also warped and/or host irregularly shaped gas at the edge of their discs. Warps and irregular features can be a sign for gas-rich minor mergers and cold gas accretion in the HIX and the control sample. Our analysis, however, suggests that the mass of detected irregular gas in HIX galaxies is not sufficient to explain their excess in H I.

(iii) HIX galaxies have a higher H I and thus baryonic specific angular momentum than control galaxies. Thus, HIX galaxies are consistent with the relation between global stability and atomic to baryonic mass fraction by Obreschkow et al. (2016). This suggests that HIX galaxies host as much H I as they can support with their baryonic specific angular momentum. A comparison to the DARK SAGE semi-analytic model (Stevens et al. 2016) suggests that the majority of the HIX galaxies have an elevated baryonic specific angular momentum because they tend to live in higher spin haloes than the majority of the control galaxies. Those HIX galaxies that do not live in intrinsically high spin haloes might have increased their specific angular momentum over their live time through strong stellar feedback that expels low angular momentum gas or through the accretion of high angular momentum gas. They might also be galaxies in transition, like interacting galaxy ESO245-G010, which are likely to use some of their gas in the future.

Our results indicate that HIX galaxies will continue to be HIX galaxies in the future unless they are heavily disturbed by e.g. interactions with other galaxies. We will continue to investigate the HIX galaxies by searching for further indications for the accretion of metal-poor gas (e.g. inhomogeneities or gradients in the gas-phase metallicity distribution) in optical spectra obtained for the HIX sample and by examining their environment from wide field optical imaging.

## ACKNOWLEDGMENTS

We would like to thank the anonymous referee for helpful comments that improved the paper.

KL would like to thank Toby Brown, Luca Cortese, Claudia Lagos, Attila Popping and Enrico di Theodoro for inspiring discussion and work experience students Devonie Lamb and Zac Broeren for their contribution to the exploration of the environment of ESO381-G005, ESO378-G003 and ESO208-G026.

This publication makes use of data products from the Two Micron All Sky Survey, which is a joint project of the University of Massachusetts and the Infrared Processing and Analysis Center/California Institute of Technology, funded by the National Aeronautics and Space Administration and the National Science Foundation.

TAO is part of the All-Sky Virtual Observatory (ASVO) and is funded and supported by Astronomy Australia Limited, Swinburne University of Technology and the Australian Government. The latter is provided through the Commonwealth’s Education Investment Fund and National Collaborative Research Infrastructure Strategy, particularly the National eResearch Collaboration Tools and Resources (NeCTAR) and the Australian National Data Service Projects.

The Australia Telescope Compact Array is part of the Australia Telescope National Facility which is funded by the Australian Government for operation as a National Facility managed by CSIRO.

This paper includes archived data obtained through the Australia Telescope Online Archive (<http://atoa.atnf.csiro.au>).

The Parkes telescope is part of the Australia Telescope which is funded by the Commonwealth of Australia for operation as a National Facility managed by CSIRO.

This research has made use of the NASA/IPAC Extragalactic Database (NED), which is operated by the Jet Propulsion Laboratory, California Institute of Technology, under contract with the National Aeronautics and Space Administration.

This research has made use of the VizieR catalogue access tool, CDS, Strasbourg, France. The original description of the VizieR service was published in A&AS 143, 23.

## REFERENCES

- Barnes J., Efstathiou G., 1987, *ApJ*, 319, 575  
 Baugh C. M., 2006, *Reports Prog. Phys.*, 69, 3101  
 Bernyk M., et al., 2016, *ApJS*, 223, 9  
 Bershaday M., Verheijen M., Swaters R., Andersen D., Westfall K., Martinsson T., 2010, *ApJ*, 716, 198  
 Bett P., Eke V., Frenk C. S., Jenkins A., Okamoto T., 2010, *MNRAS*, 404, 1137  
 Birnboim Y., Dekel A., 2003, *MNRAS*, 345, 349  
 Bournaud F., Combes F., Jog C. J., Puerari I., 2005, *A&A*, 438, 507  
 Broeils A. H., Rhee M.-H., 1997, *A&A*, 324, 877  
 Brown T., Catinella B., Cortese L., Kilborn V., Haynes M., Giovanelli R., 2015, *MNRAS*, 452, 2479  
 Bruzual G., Charlot S., 2003, *MNRAS*, 344, 1000  
 Bullock J. S., Dekel A., Kolatt T. S., Kravtsov A. V., Klypin A. A., Porciani C., Primack J. R., 2001, *ApJ*, 555, 240  
 Catinella B., et al., 2010, *MNRAS*, 403, 683  
 Chabrier G., 2003, *PASP*, 115, 763  
 Cortese L., et al., 2014, *ApJ*, 795, L37  
 Cortese L., et al., 2016, *MNRAS*, 463, 170  
 Dalcanton J. J., Spergel D. N., Summers F. J., 1997, *ApJ*, 482, 659  
 Dekel A., Birnboim Y., 2006, *MNRAS*, 368, 2  
 Dénes H., Kilborn V., Koribalski B., 2014, *MNRAS*, 444, 667  
 Di Teodoro E. M., Fraternali F., 2014, *A&A*, 567, 68  
 Doyle M., et al., 2005, *MNRAS*, 361, 34  
 Dreyer J. L. E., 1888, *MmRAS*, 49, 1  
 Dreyer J. L. E., 1910, *MmRAS*, 59, 105  
 Fall S. M., Efstathiou G., 1980, *MNRAS*, 193, 189  
 Flynn C., Holmberg J., Portinari L., Fuchs B., Jahreiß H., 2006, *MNRAS*, 372, 1149  
 Forbes J., Krumholz M., Burkert A., Dekel A., 2014, *MNRAS*, 438, 1552  
 Fraternali F., Sancisi R., Kamphuis P., 2011, *A&A*, 531, 64  
 Genel S., Fall S., Hernquist L., Vogelsberger M., Snyder G.,

- Rodriguez-Gomez V., Sijacki D., Springel V., 2015, *ApJ*, 804, L40
- Gentile G., Józsa G. I. G., Serra P., Heald G. H., de Blok W. J. G., Fraternali F., Patterson M. T., 2013, *A&A*, 554, 125
- Giovanelli R., et al., 2005, *AJ*, 130, 2598
- Hallenbeck G., et al., 2014, *AJ*, 148, 69
- Hallenbeck G., et al., 2016, *AJ*, 152, 225
- Heald G. H., 2015, in Ziegler B., Combes F., Danerbauer H., Verdugo M., eds, IAU Symposium Vol. 309, Galaxies 3D across Universe. pp 69–72 ([arXiv:1409.7599](https://arxiv.org/abs/1409.7599)), doi:10.1017/S1743921314009338, <http://adsabs.harvard.edu/abs/2015IAUS...309...69H>
- Heald G., et al., 2011, *A&A*, 526, 118
- Huang S., et al., 2014, *ApJ*, 793, 40
- Józsa G. I. G., 2007, *A&A*, 468, 903
- Józsa G. I. G., Kenn F., Klein U., Oosterloo T. A., 2007, *A&A*, 468, 731
- Kalberla P. M. W., Dedes L., 2008, *A&A*, 487, 951
- Kennicutt R. C. J., 1998, *ApJ*, 498, 541
- Kereš D., Katz N., Weinberg D., Davé R., 2005, *MNRAS*, 363, 2
- Kilborn V. A., Forbes D. A., Koribalski B. S., Brough S., Kern K., 2006, *MNRAS*, 371, 739
- Kim J.-h., Lee J., 2013, *MNRAS*, 432, 1701
- Koribalski B. S., et al., 2004, *AJ*, 128, 16
- Lagos C. d. P., et al., 2017a, eprint arXiv
- Lagos C., Theuns T., Stevens A., Cortese L., Padilla N., Davis T., Contreras S., Croton D., 2017b, *MNRAS*, 464, 3850
- Lange R., et al., 2015, *MNRAS*, 447, 2603
- Lauberts A., Valentijn E., 1989, The surface photometry catalogue of the ESO-Uppsala galaxies
- Leroy A. K., Walter F., Brinks E., Bigiel F., de Blok W. J. G., Madore B., Thornley M. D., 2008, *AJ*, 136, 2782
- Li Z.-Y., Ho L. C., Barth A. J., Peng C. Y., 2011, *ApJS*, 197, 22
- Lutz K., et al., 2017, *MNRAS*, 467, 1083
- Maddox N., Hess K., Obreschkow D., Jarvis M., Blyth S.-L., 2015, *MNRAS*, 447, 1610
- McMillan P., 2011, *MNRAS*, 414, 2446
- Meurer G. R., 2017, *Form. Evol. Galaxy Outskirts, Proc. Int. Astron. Union, IAU Symp. Vol. 321, pp. 172-179*, 321, 172
- Meyer M., et al., 2004, *MNRAS*, 350, 1195
- Mo H. J., Mao S., White S. D. M., 1998, *MNRAS*, 295, 319
- Moran S., et al., 2012, *ApJ*, 745, 66
- Obreschkow D., Glazebrook K., 2014, *ApJ*, 784, 26
- Obreschkow D., Glazebrook K., Kilborn V., Lutz K., 2016, *ApJ*, 824, L26
- Oosterloo T., Fraternali F., Sancisi R., 2007, *AJ*, 134, 1019
- Peebles P., 1969, *ApJ*, 155, 393
- Putman M., Peek J., Jong M., 2012, *ARA&A*, 50, 491
- Rogstad D. H., Lockart I. A., Wright M. C. H., 1974, *ApJ*, 193, 309
- Romanowsky A., Fall S., 2012, *ApJS*, 203, 17
- Roškar R., Debattista V., Brooks A., Quinn T., Brook C., Governato F., Dalcanton J., Wadsley J., 2010, *MNRAS*, 408, 783
- Saintonge A., et al., 2011, *MNRAS*, 415, 32
- Sánchez Almeida J., Elmegreen B. G., Muñoz-Tuñón C., Elmegreen D. M., 2014, *A&A Rv*, 22, 71
- Sancisi R., Fraternali F., Oosterloo T., Van Der Hulst T., 2008, *A&A Rv*, 15, 189
- Sanders D. B., Solomon P. M., Scoville N. Z., 1984, *ApJ*, 276, 182
- Sault R., Teuben P., Wright M., 1995, in Shaw R., Payne H., Hayes J., eds, Astronomical Society of the Pacific Conference Series Vol. 77, Astron. Data Anal. Softw. Syst. IV. p. 433
- Schiminovich D., et al., 2010, *MNRAS*, 408, 919
- Shaw L. D., Weller J., Ostriker J. P., Bode P., 2006, *ApJ*, 646, 815
- Skrutskie M. F., et al., 2006, *AJ*, 131, 1163
- Somerville R. S., Davé R., 2015, *ARA&A*, 53, 51
- Spergel D. N., et al., 2003, *ApJS*, 148, 175
- Springel V., et al., 2005, *Nature*, 435, 629
- Stevens A., Croton D., Mutch S., 2016, *MNRAS*, 461, 859
- Stevens A. R. H., Lagos C. d. P., Contreras S., Croton D. J., Padilla N. D., Schaller M., Schaye J., Theuns T., 2017, *MNRAS*, 467, 2066
- Stewart K., Kaufmann T., Bullock J., Barton E., Maller A., Diemand J., Wadsley J., 2011, *ApJ*, 738, 39
- Stewart K., Brooks A., Bullock J., Maller A., Diemand J., Wadsley J., Moustakas L., 2013, *ApJ*, 769, 74
- Stewart K., et al., 2016, eprint arXiv
- Toomre A., 1964, *ApJ*, 139, 1217
- Übler H., Naab T., Oser L., Aumer M., Sales L., White S., 2014, *MNRAS*, 443, 2092
- Walsh W., Staveley-Smith L., Oosterloo T., 1997, *AJ*, 113, 1591
- Walter F., Brinks E., de Blok W. J. G., Bigiel F., Kennicutt R. C., Thornley M. D., Leroy A. K., 2008, *AJ*, 136, 2563
- Wang J., et al., 2014, *MNRAS*, 441, 2159
- Wang J., Koribalski B. S., Serra P., van der Hulst T., Roychowdhury S., Kamphuis P., Chengalur J. N., 2016, *MNRAS*, 460, 2143
- Wen X.-Q., Wu H., Zhu Y.-N., Lam M. I., Wu C.-J., Wicker J., Zhao Y.-H., 2013, *MNRAS*, 433, 2946
- White S. D. M., Rees M. J., 1978, *MNRAS*, 183, 341
- Wilson W., et al., 2011, *MNRAS*, 416, 832
- Wong O., Meurer G., Zheng Z., Heckman T., Thilker D., Zwaan M., 2016, *MNRAS*, 460, 1106
- Wright A., Otrupcek R., 1990, in PKS Cat..
- Zjupa J., Springel V., 2017, *MNRAS*, 466, 1625
- Zschaechner L., Rand R., Heald G., Gentile G., Kamphuis P., 2011, *ApJ*, 740, 35
- Zschaechner L., Rand R., Heald G., Gentile G., Józsa G., 2012, *ApJ*, 760, 37
- Zwaan M., Meyer M., Staveley-Smith L., Webster R., 2005, *MNRAS*, 359, L30
- de Blok W. J. G., et al., 2014, *A&A*, 566, 80
- de Vaucouleurs G., de Vaucouleurs A., Corwin Jr. H., Buta R., Paturel G., Fouqué P., 1991, Third Reference Catalogue of Bright Galaxies. Volume I: Explanations and references. Volume II: Data for galaxies between 0h and 12h. Volume III: Data for galaxies between 12h and 24h. <http://adsabs.harvard.edu/abs/1991rc3..book.....D>
- van de Voort F., Schaye J., Booth C., Haas M., Dalla Vecchia C., 2011, *MNRAS*, 414, 2458

**APPENDIX A: ATCA HI DATA OF THE HIX SAMPLE**

In this and the following section we present the data of the HIX and the control sample respectively that has been used in this paper. For each galaxy, there are eight panels:

Panel (a): the ATCA integrated H I intensity (moment 0) map overlaid on the optical *B-band* image from SuperCOSMOS. The contours are starting at  $0.4 \times 10^{20}$  and  $0.8 \times 10^{20} \text{ cm}^{-2}$  for the HIX and the control sample respectively and double with every step. The red ellipse in the bottom left corner shows the synthesised beam.

Panel (b): the radial profile of the H I column density as measured from elliptical annuli. The vertical solid grey line marks the H I radius  $R_{HI}$ . Horizontal, dashed lines mark  $1 M_{\odot} \text{ pc}^{-2}$ , which is the isophote for the  $R_{HI}$  measurement and  $0.4 \text{ cm}^{-2}$ , which is the order of the column density limit for HIX galaxies.

Panel (c): the ATCA mean velocity field (moment 1) map. The red ellipse in the bottom left corner shows the synthesised beam.

Panel (d): the rotation velocity measured by TiRiFiC (black dots connected by a black dashed line) and a fit to that rotation curve (grey solid line) of the functional form:

$$v_{\text{rot}}(r) = v_{\text{flat}} \cdot \left[ 1 - \exp\left(\frac{-r}{l_{\text{flat}}}\right) \right] \quad (\text{A1})$$

Panel (e): H I spectra as measured from the ATCA data cube (black solid line), from the HIPASS cube (grey solid line) and the residual between the input data cube and the TiRiFiC model cube (grey dashed line).

Panel (f): the radial variation of the inclination (black dots and dashed line, left y-axis) and the position angle (grey dots and dashed line, right y-axis) as modelled by TiRiFiC.

Panel (g): a position velocity diagram along the minor axis. Blue contours and grey scale background present the data cube and red contours the TiRiFiC model cube.

Panel (h): a position velocity diagram along the major axis. Colour coding as in Panel (g).

**APPENDIX B: ATCA HI DATA OF THE control SAMPLE**

This section presents the data panels of the control galaxies. The panels are structured as in App. A.

This paper has been typeset from a  $\text{\TeX}/\text{\LaTeX}$  file prepared by the author.



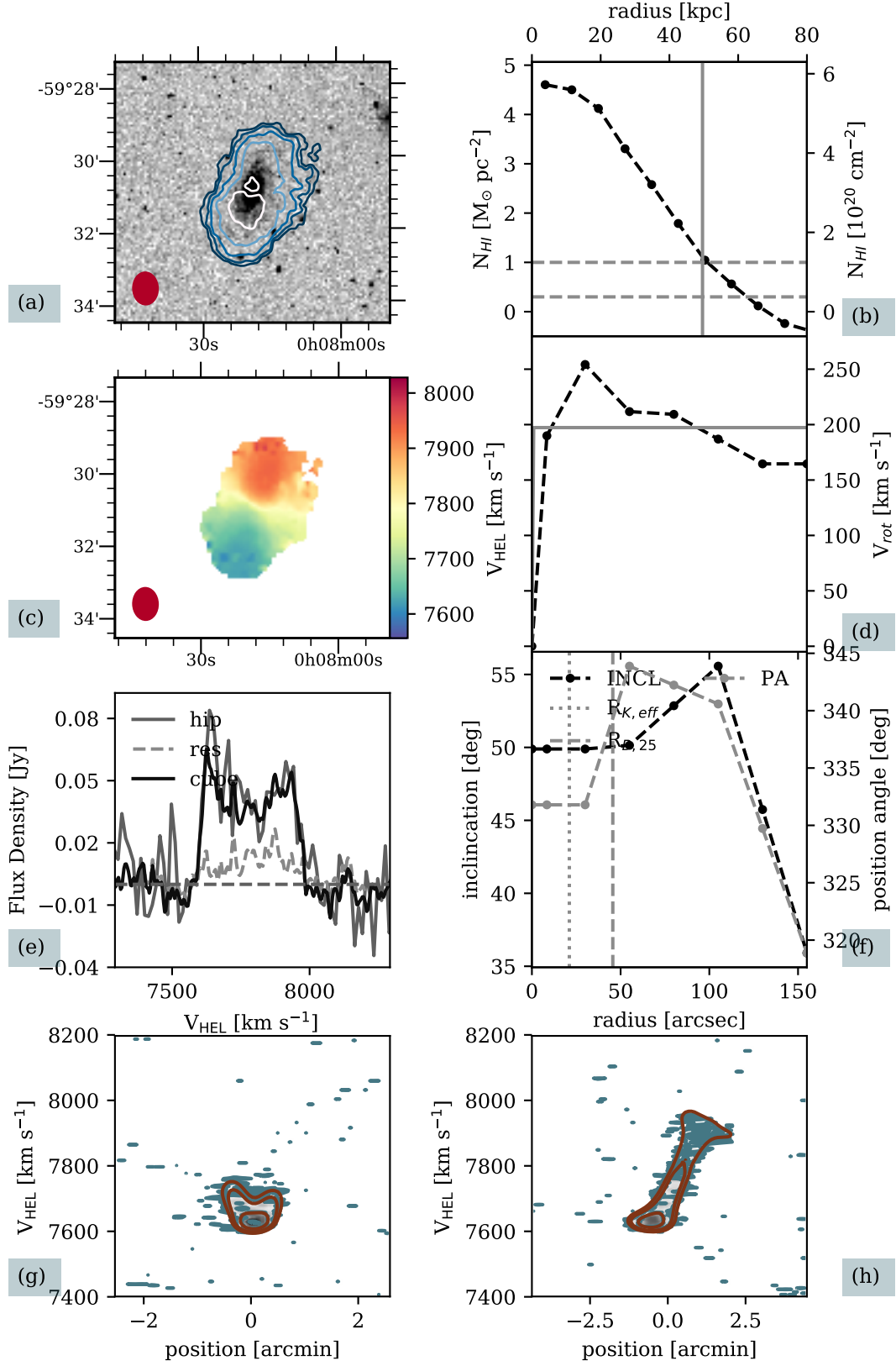


Figure A1. ESO111-G014

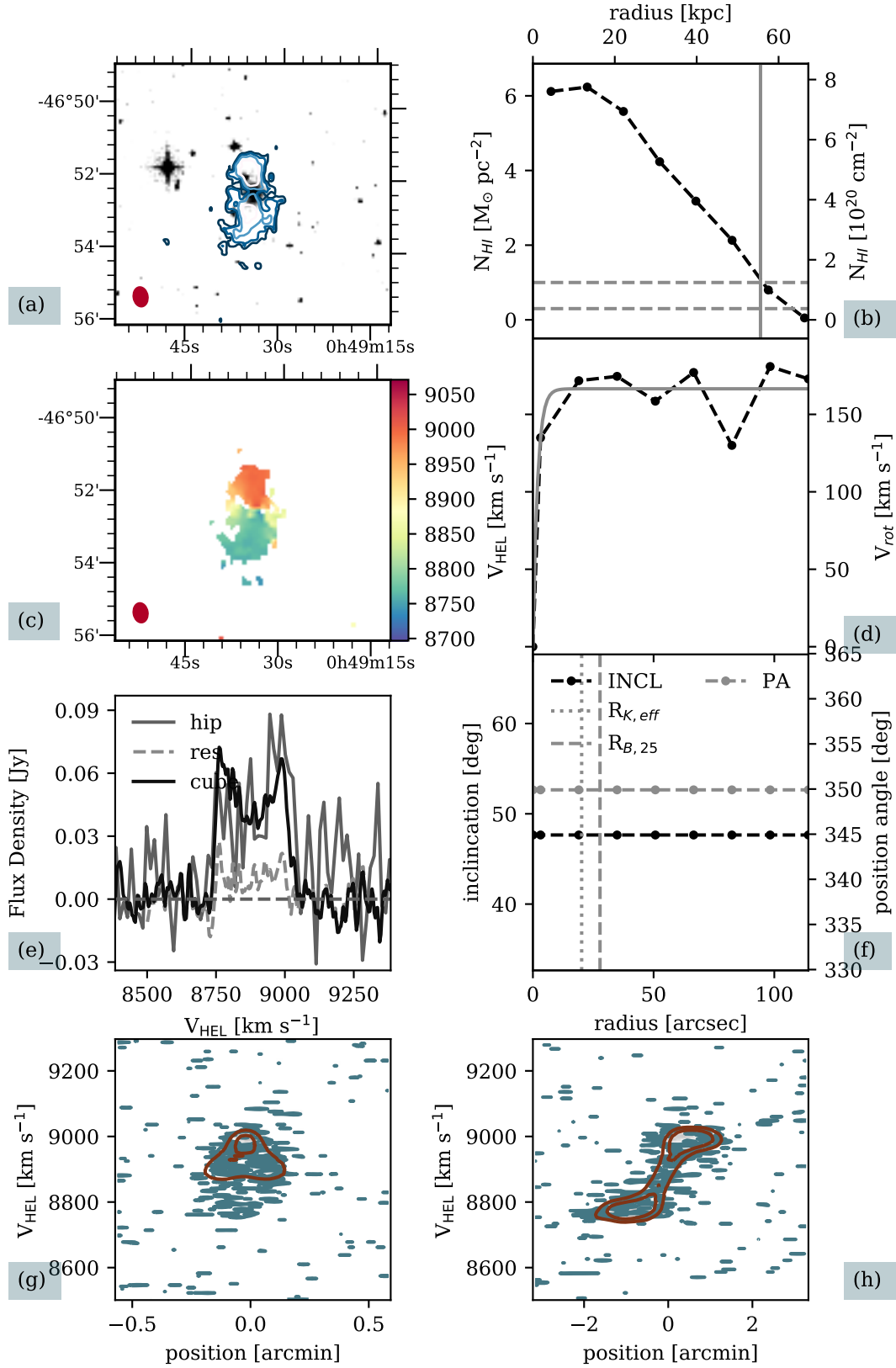


Figure A2. ESO243-G002

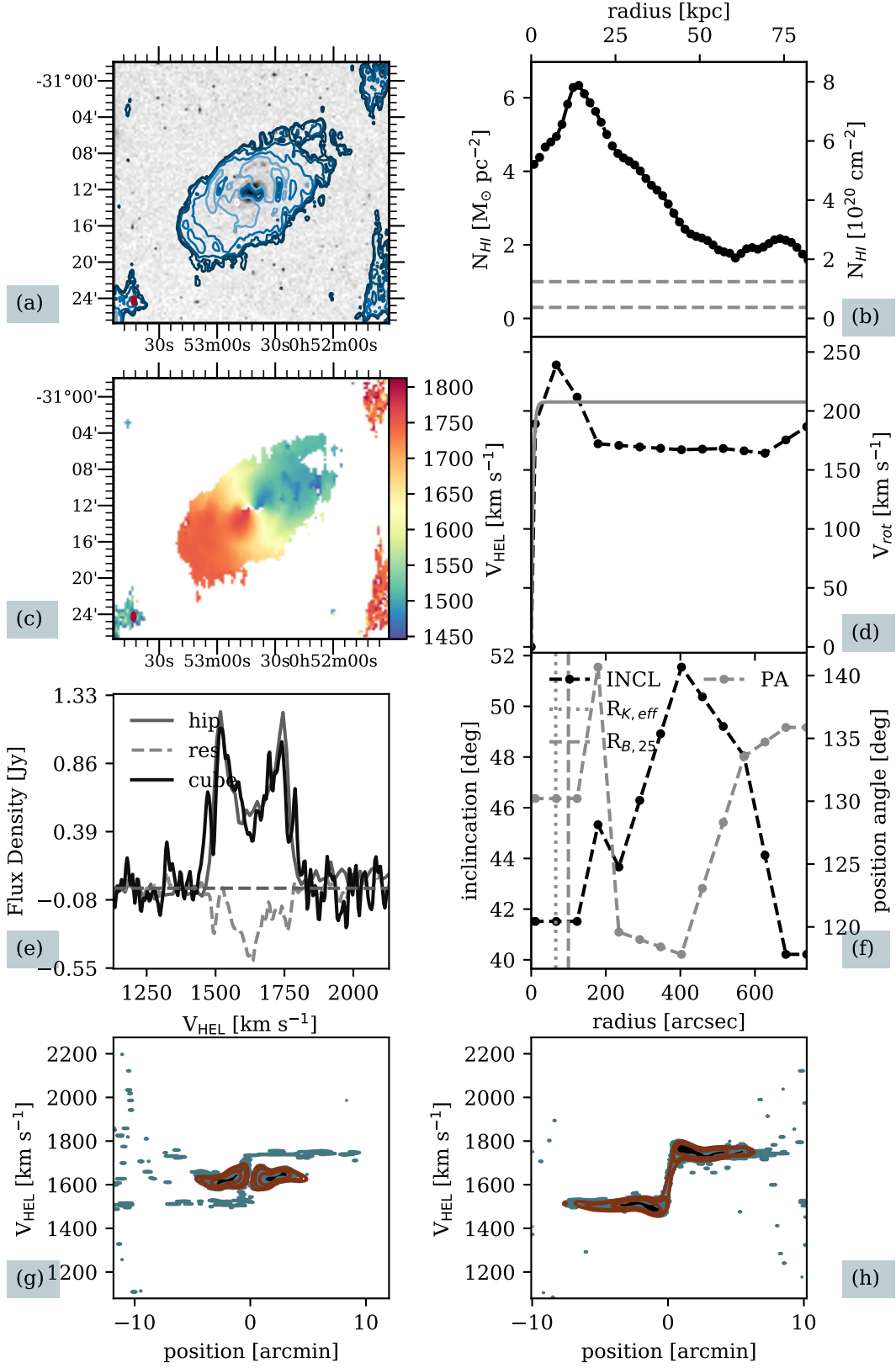


Figure A3. NGC289

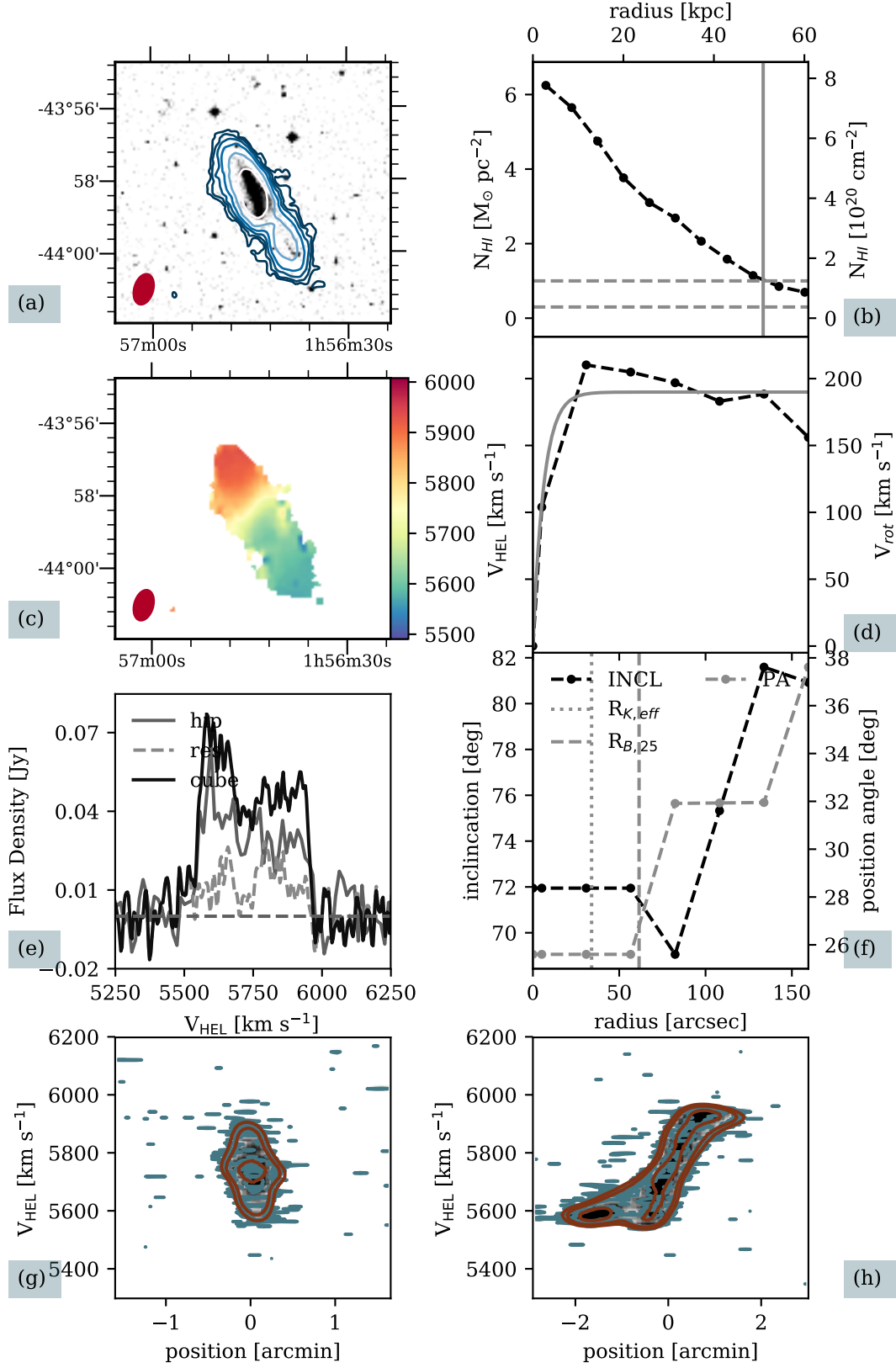


Figure A4. ESO245-G010

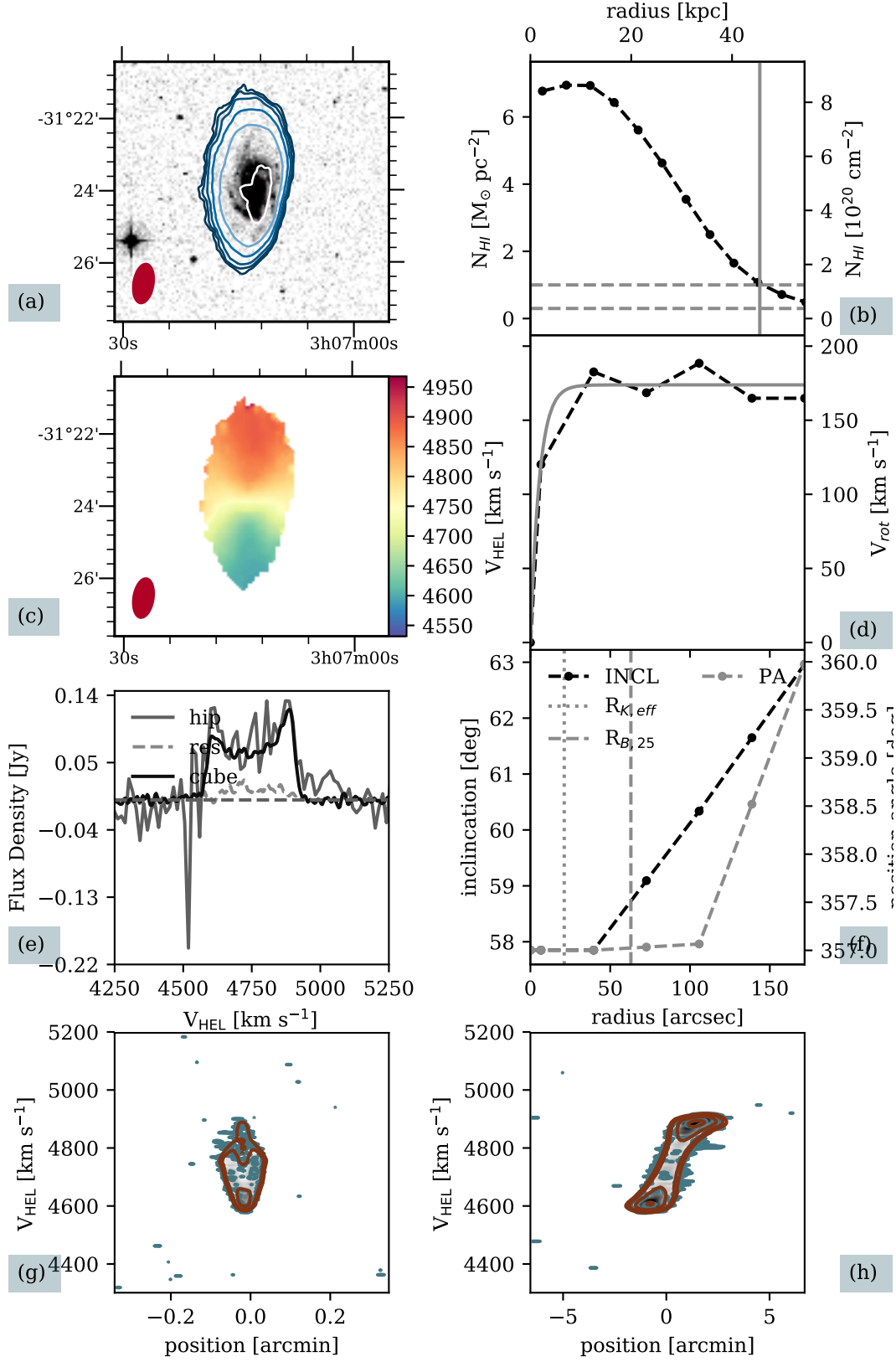


Figure A5. ESO417-G018

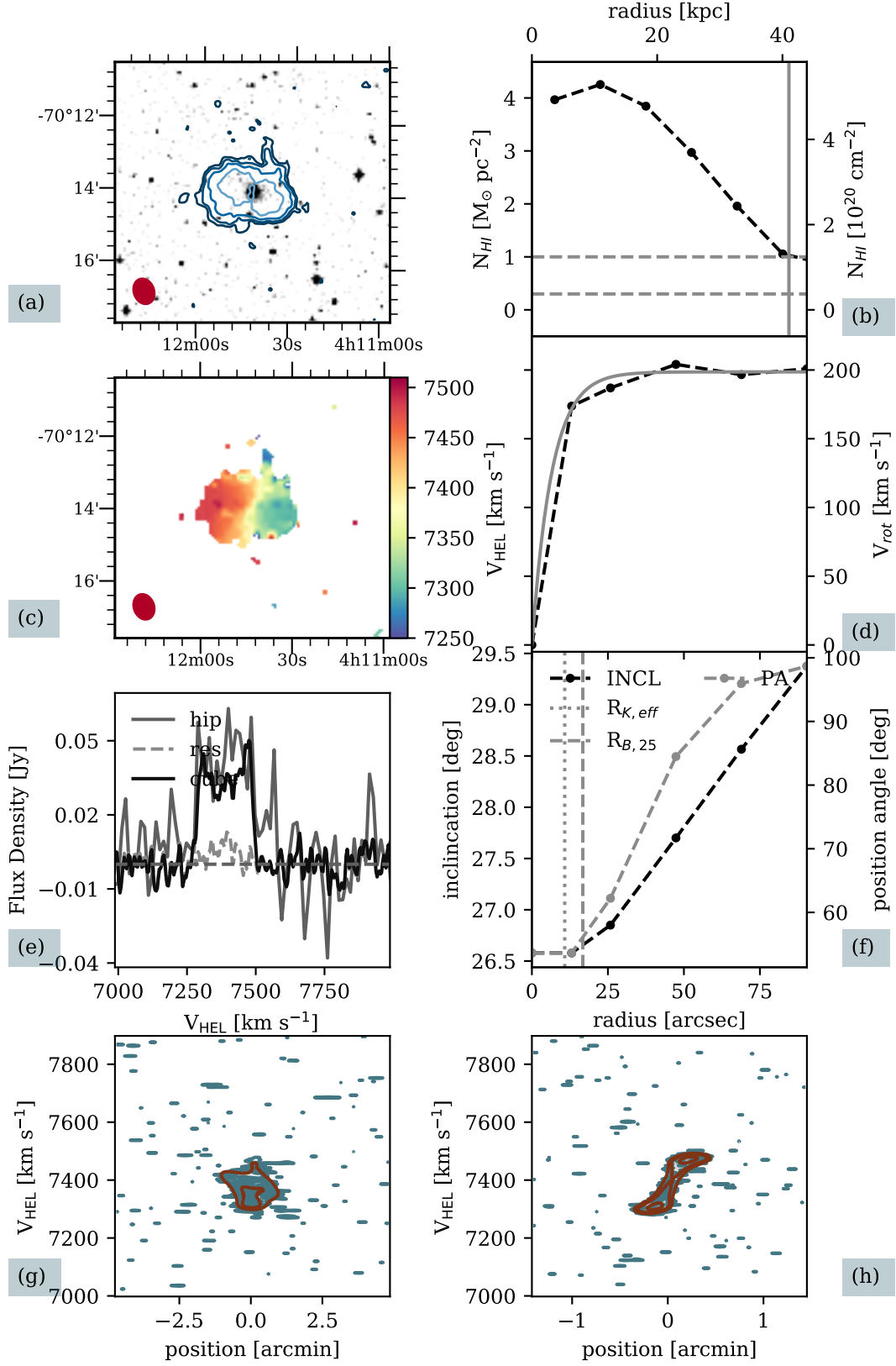


Figure A6. ESO055-G013

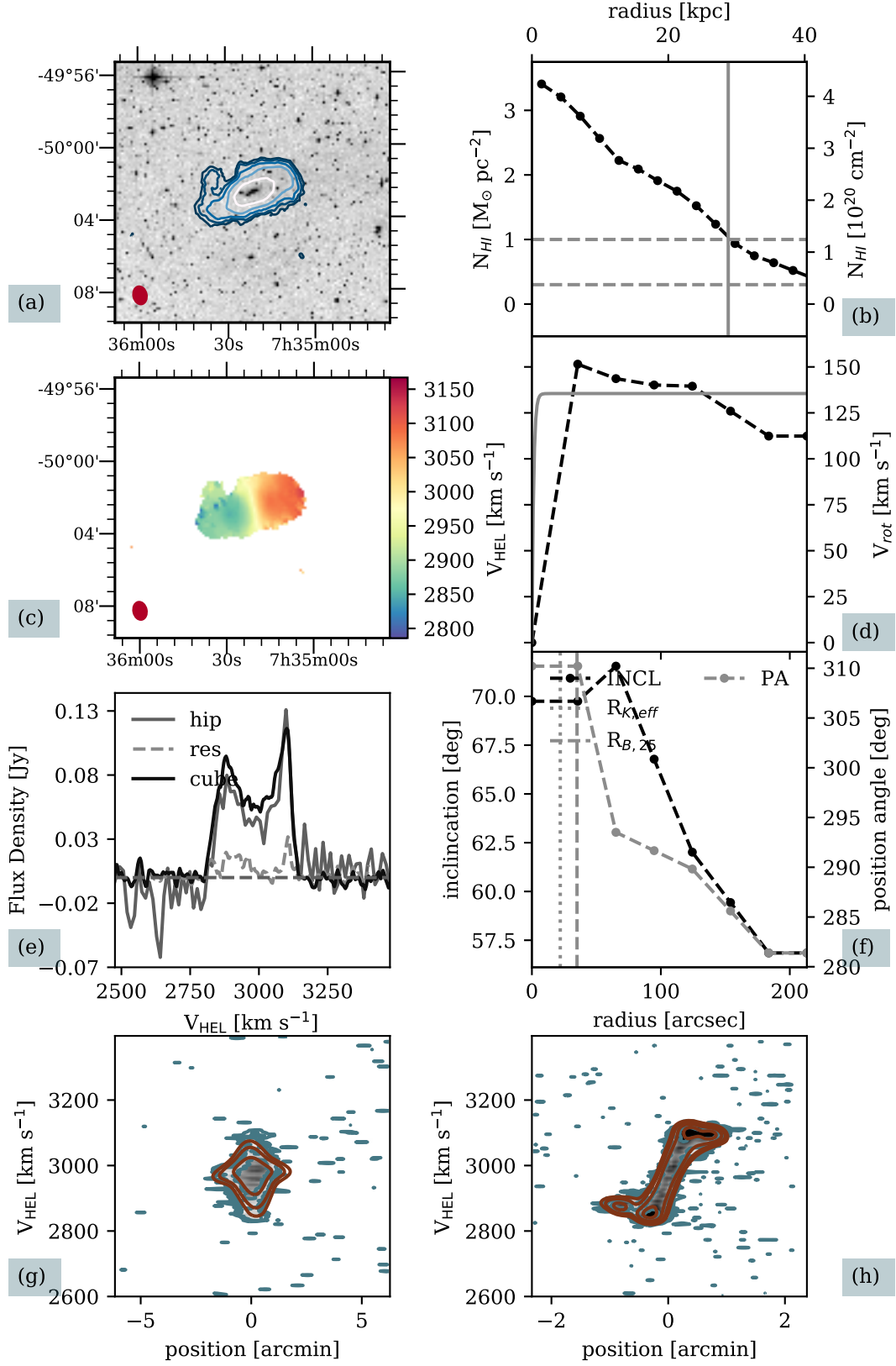


Figure A7. ESO208-G026

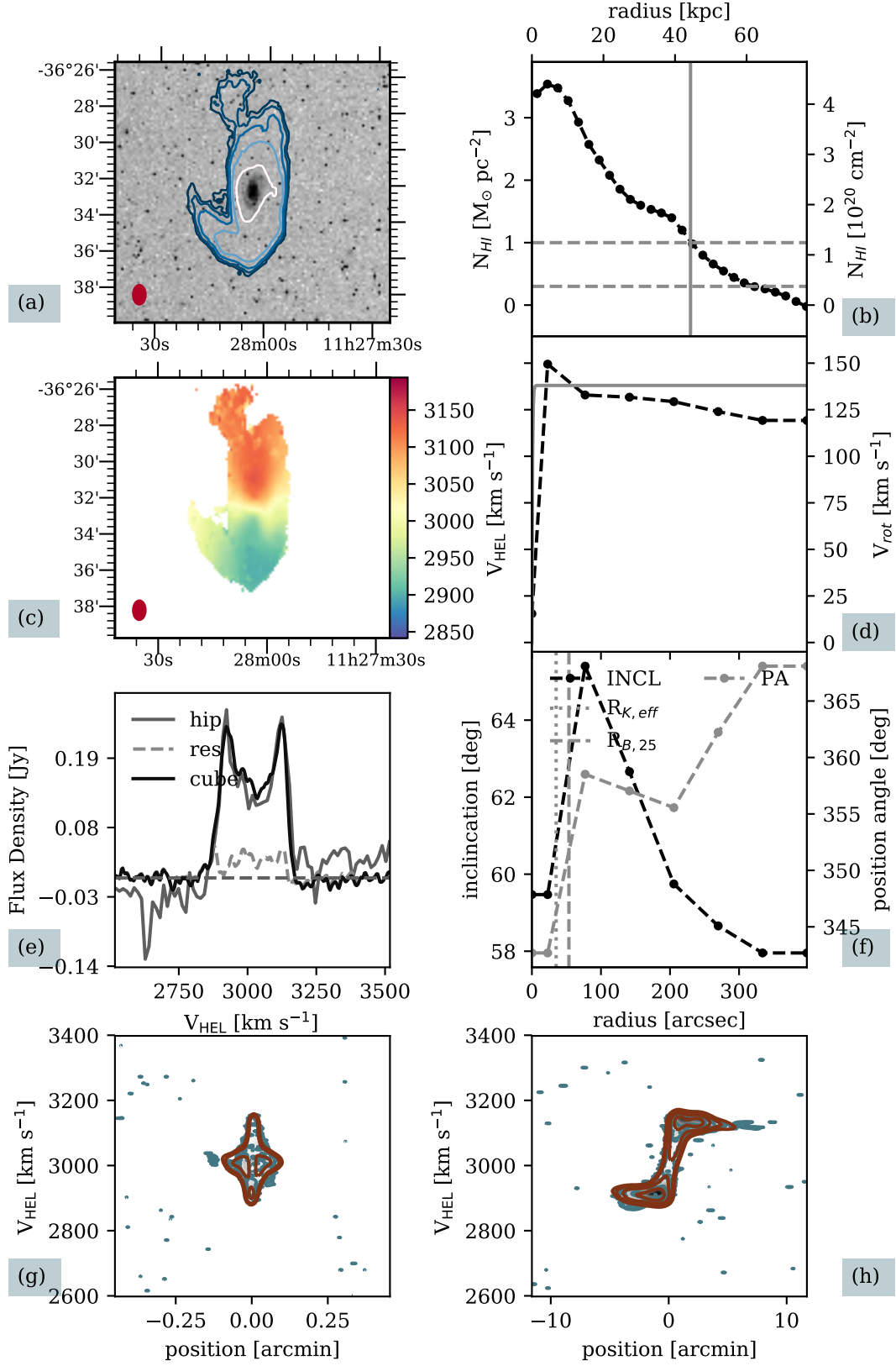


Figure A8. ESO378-G003



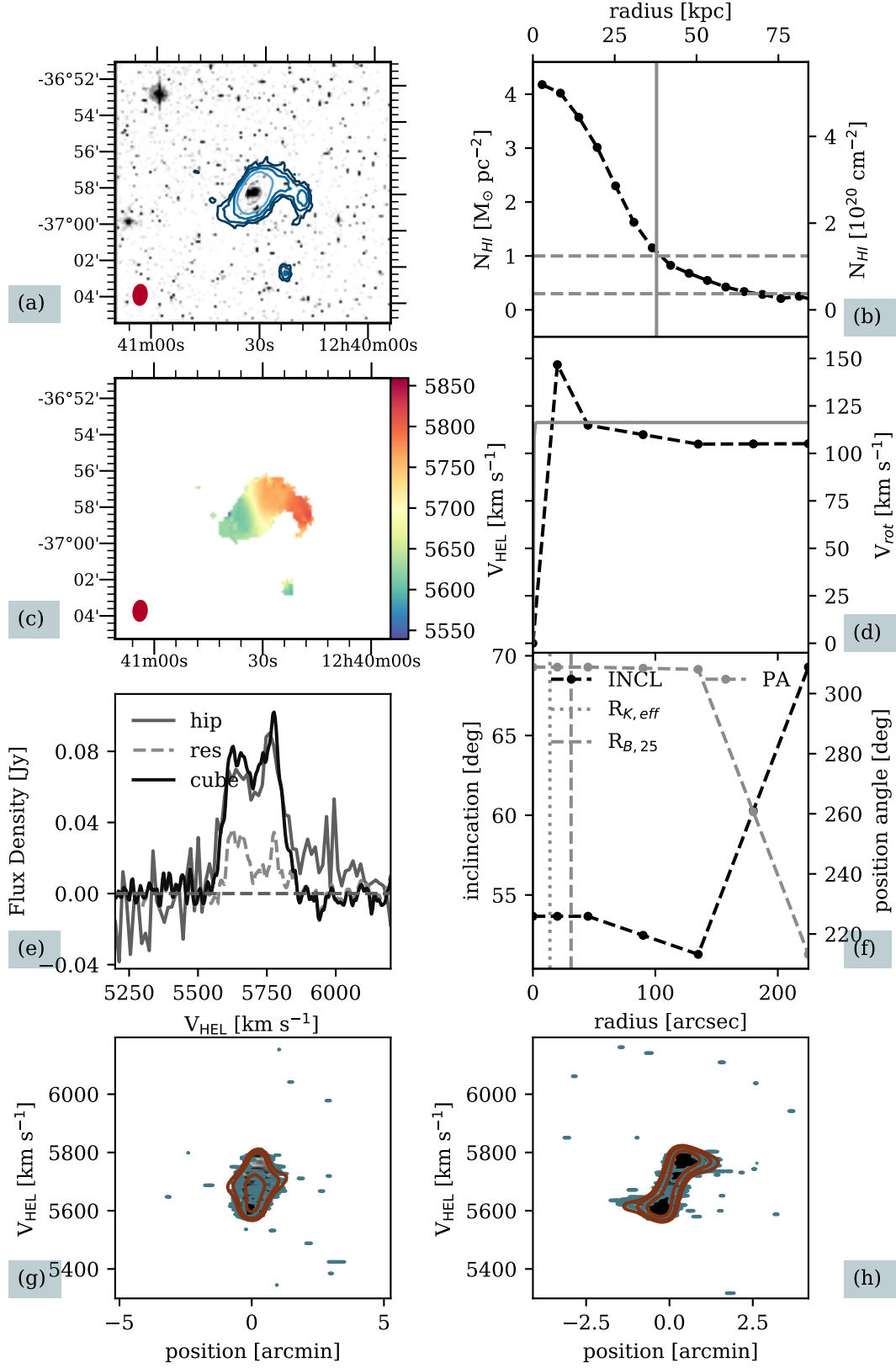


Figure A9. ESO381-G005

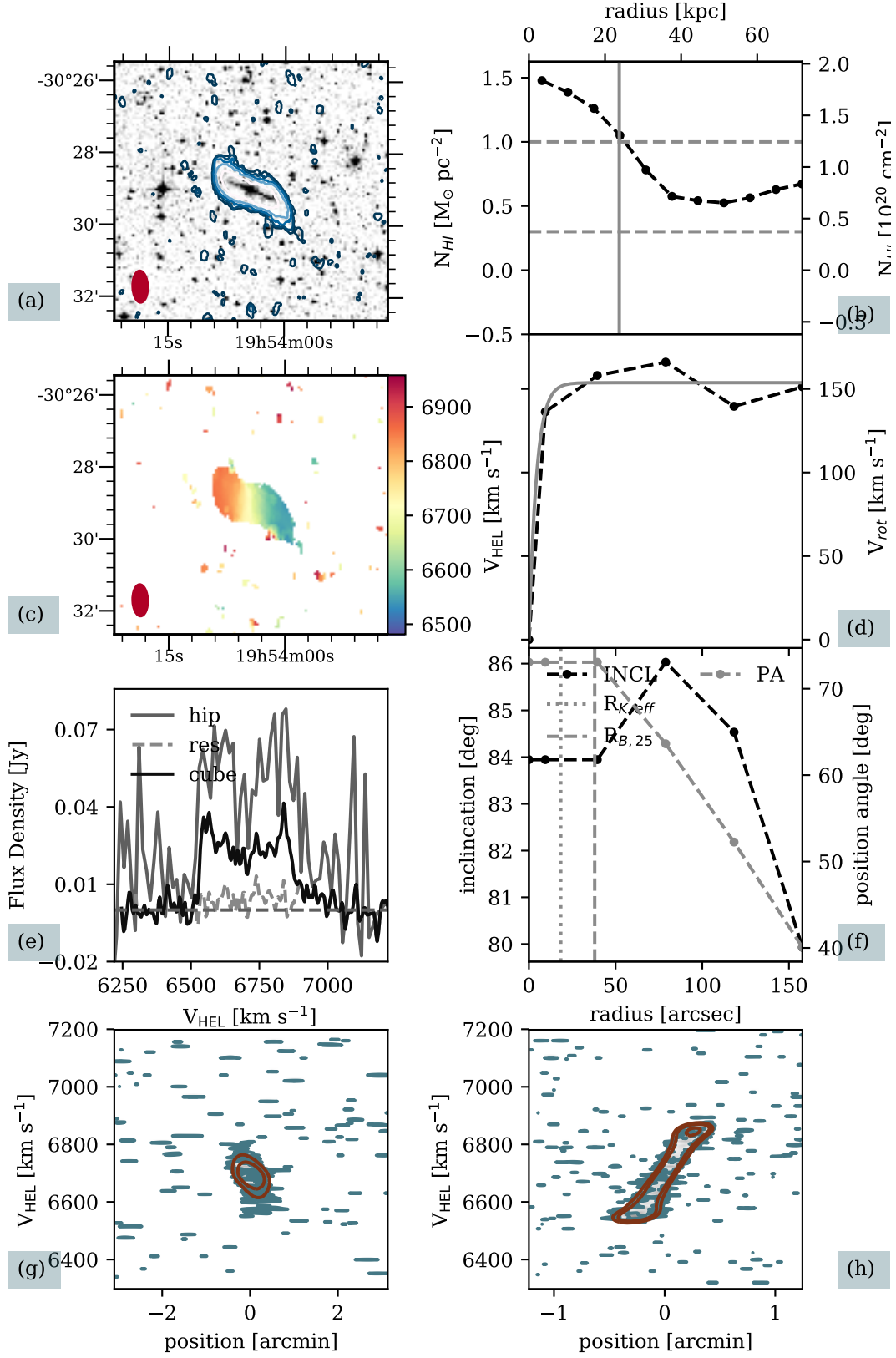


Figure A10. ESO461-G010

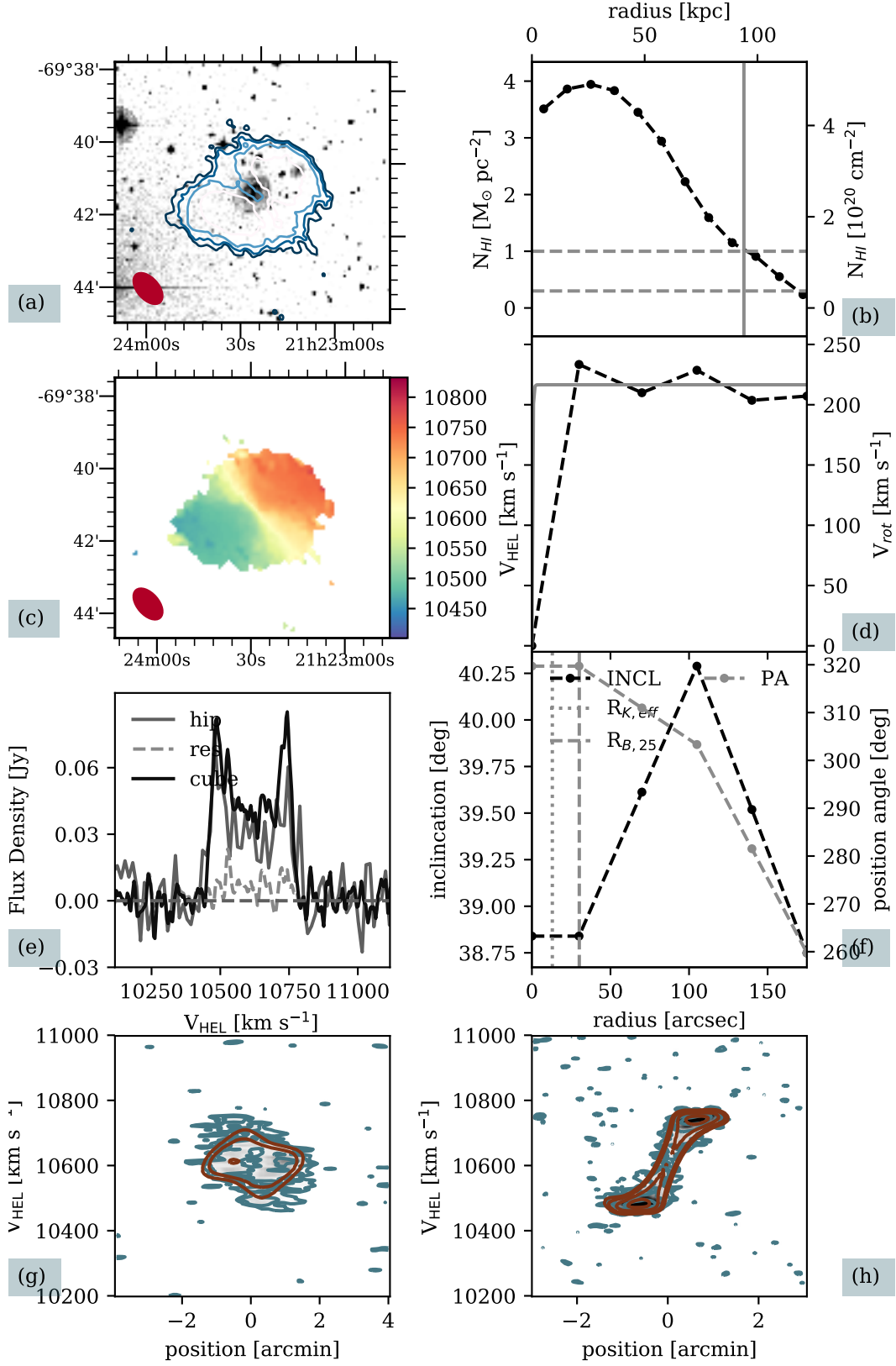


Figure A11. ESO075-G006

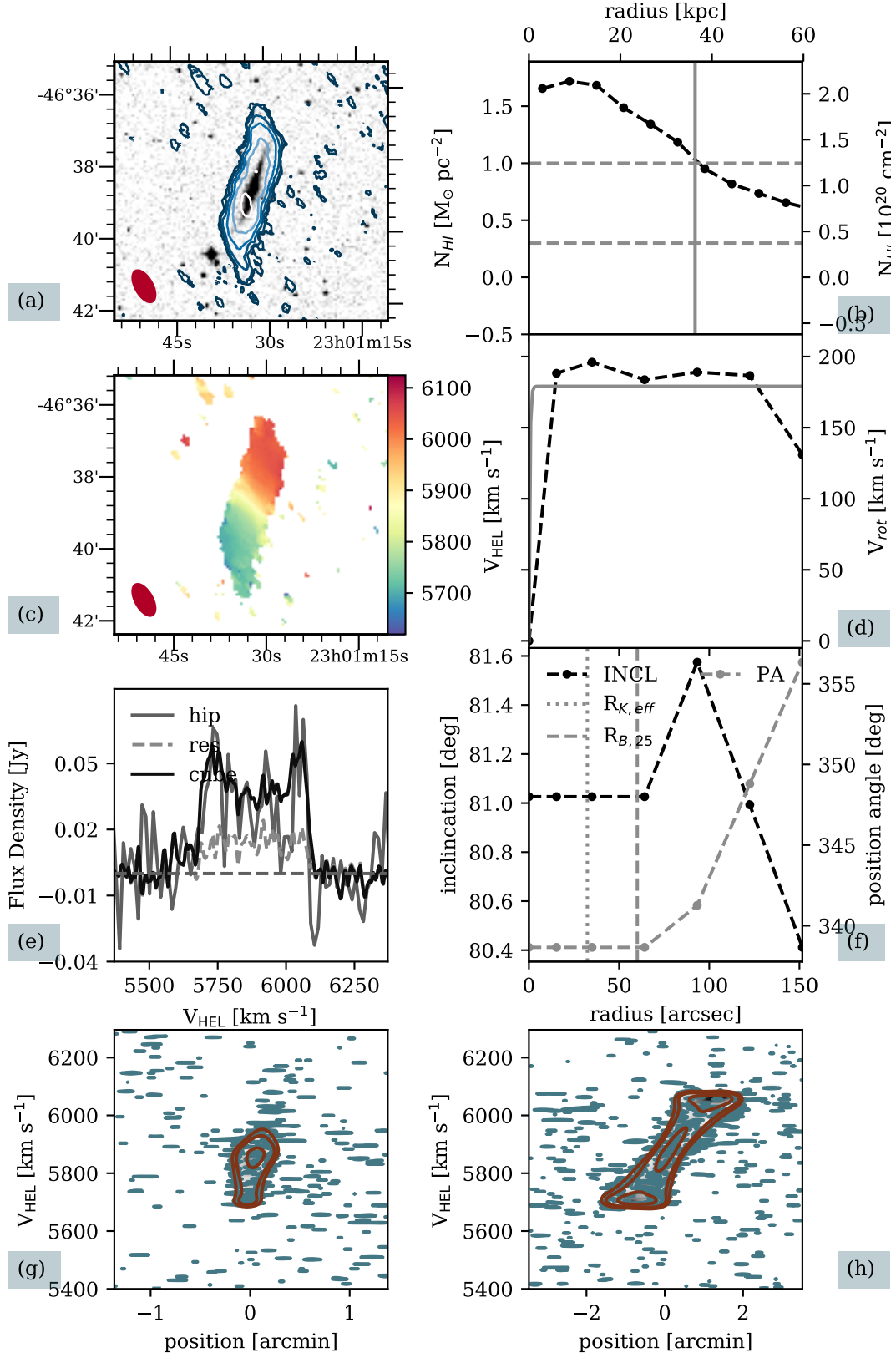


Figure A12. ESO290-G035

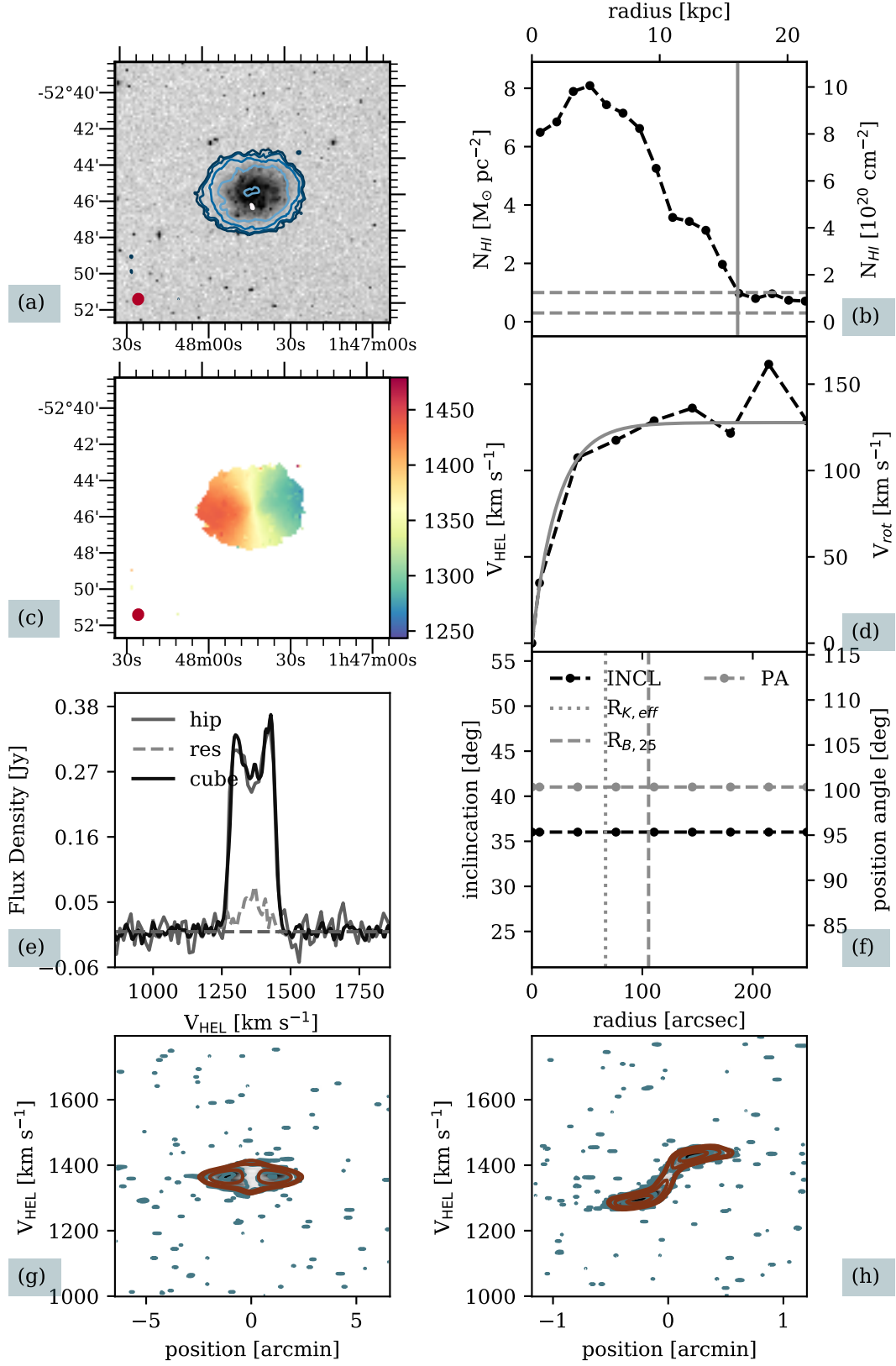


Figure B1. NGC685

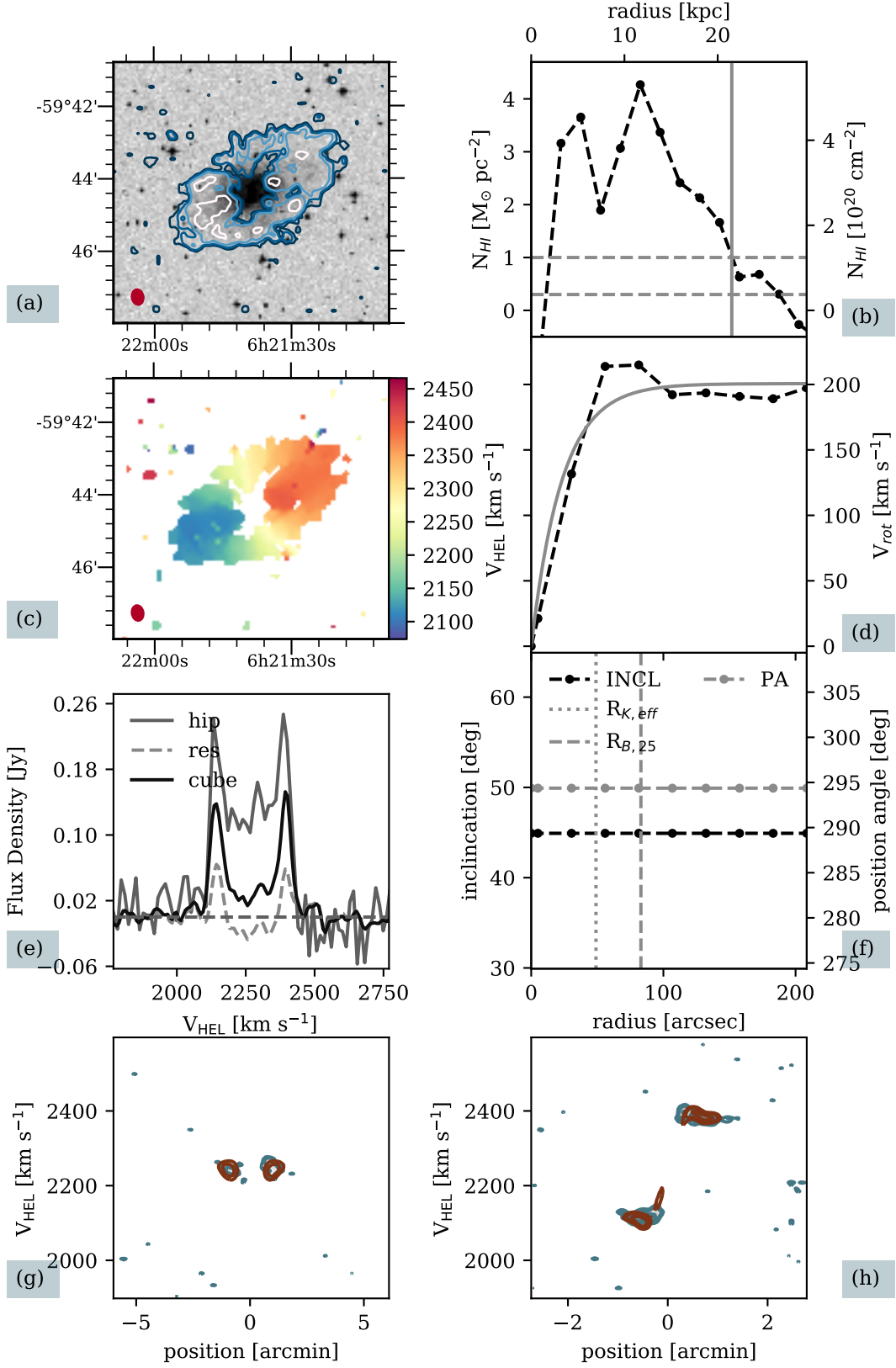


Figure B2. ESO121-G026

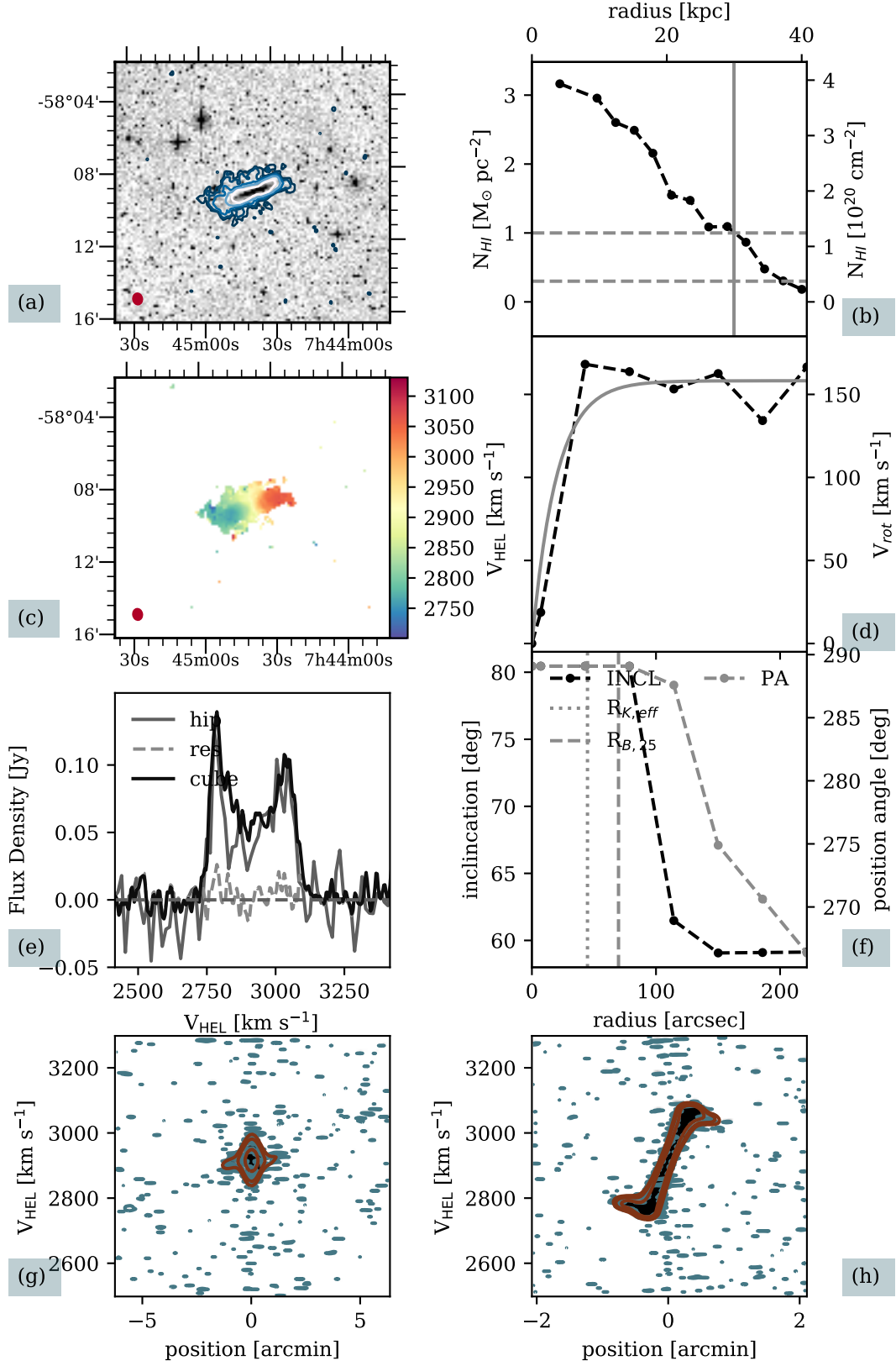


Figure B3. ESO123-G023

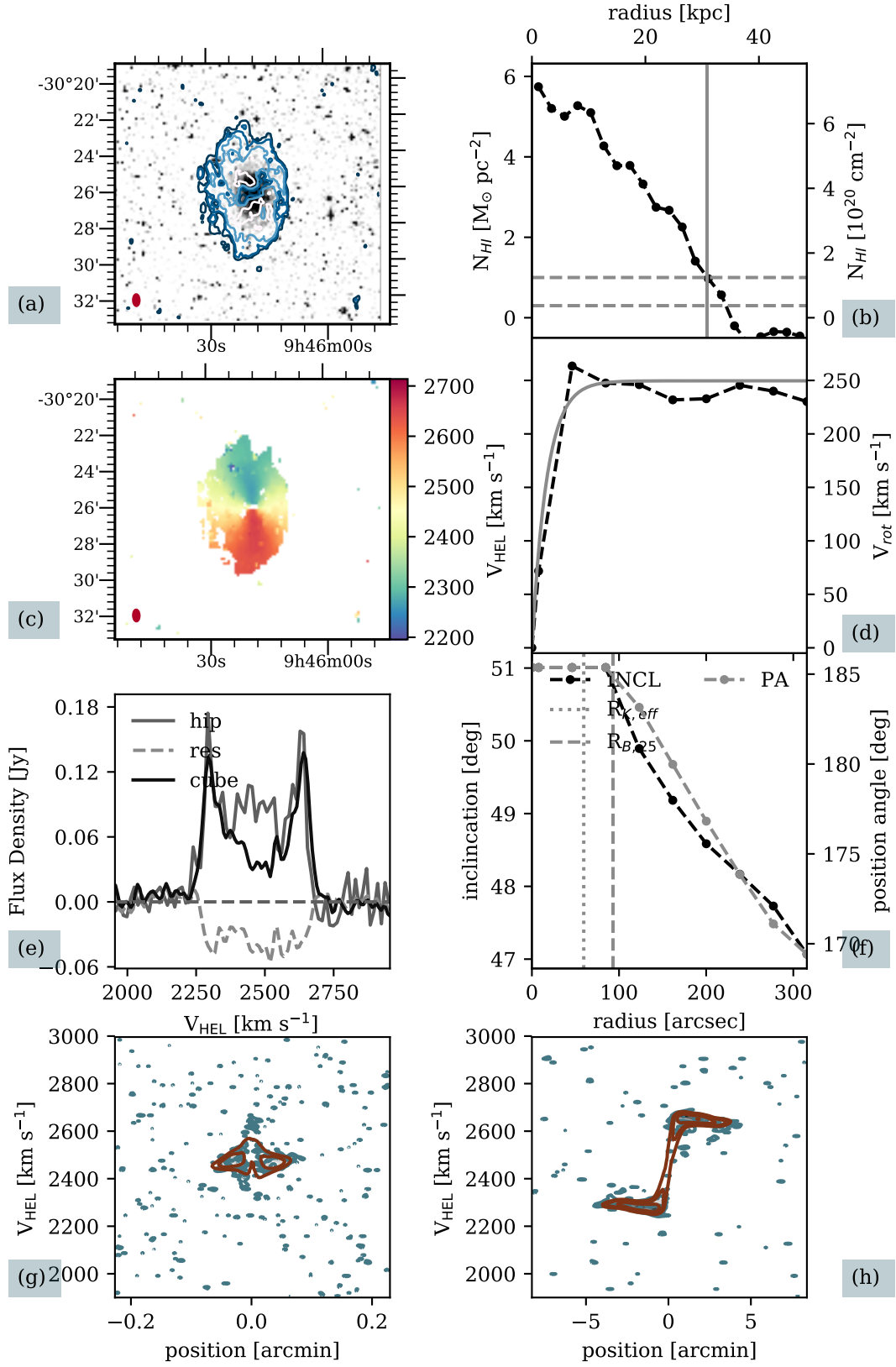


Figure B4. NGC3001



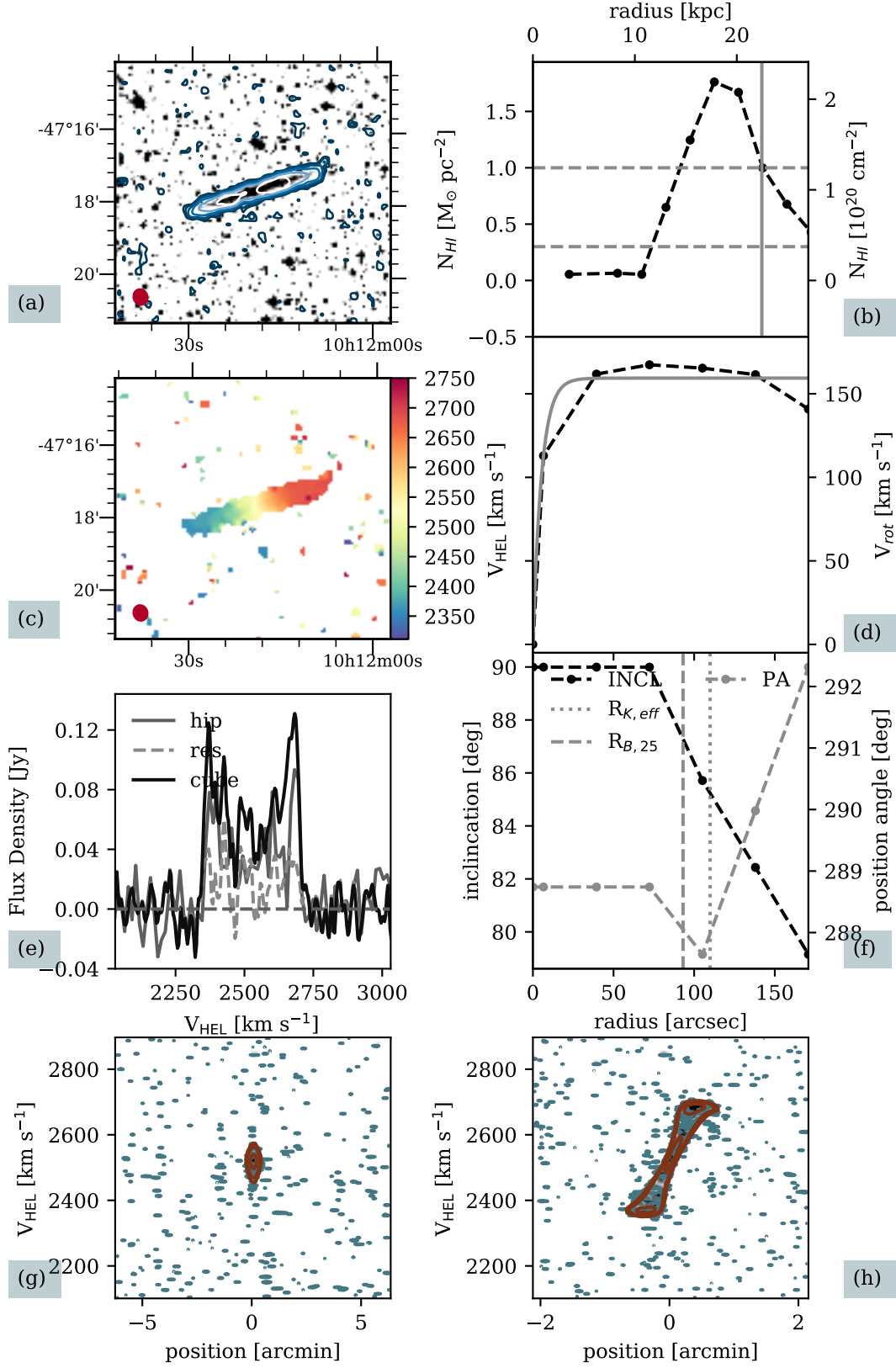


Figure B5. ESO263-G015

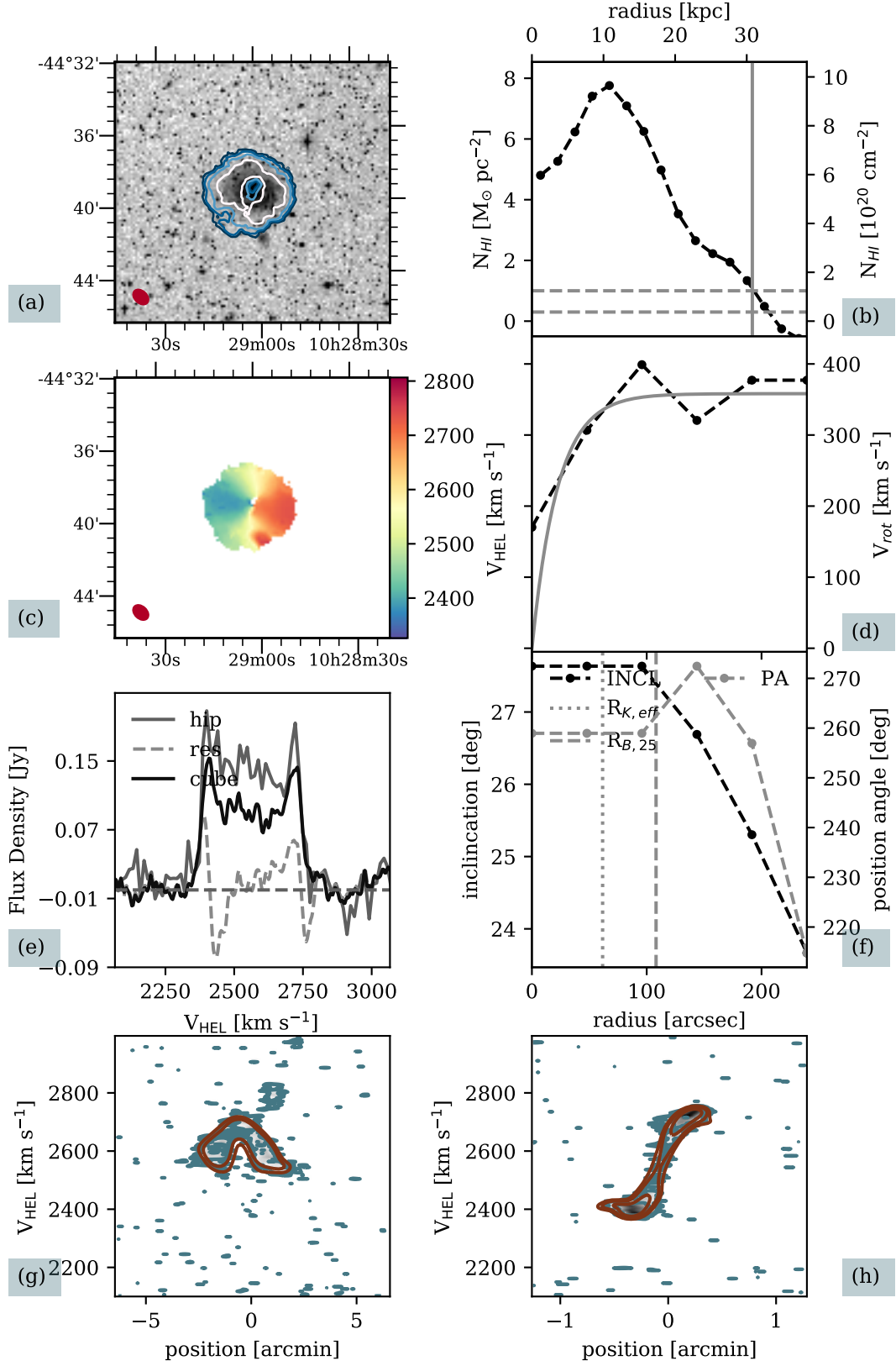


Figure B6. NGC3261

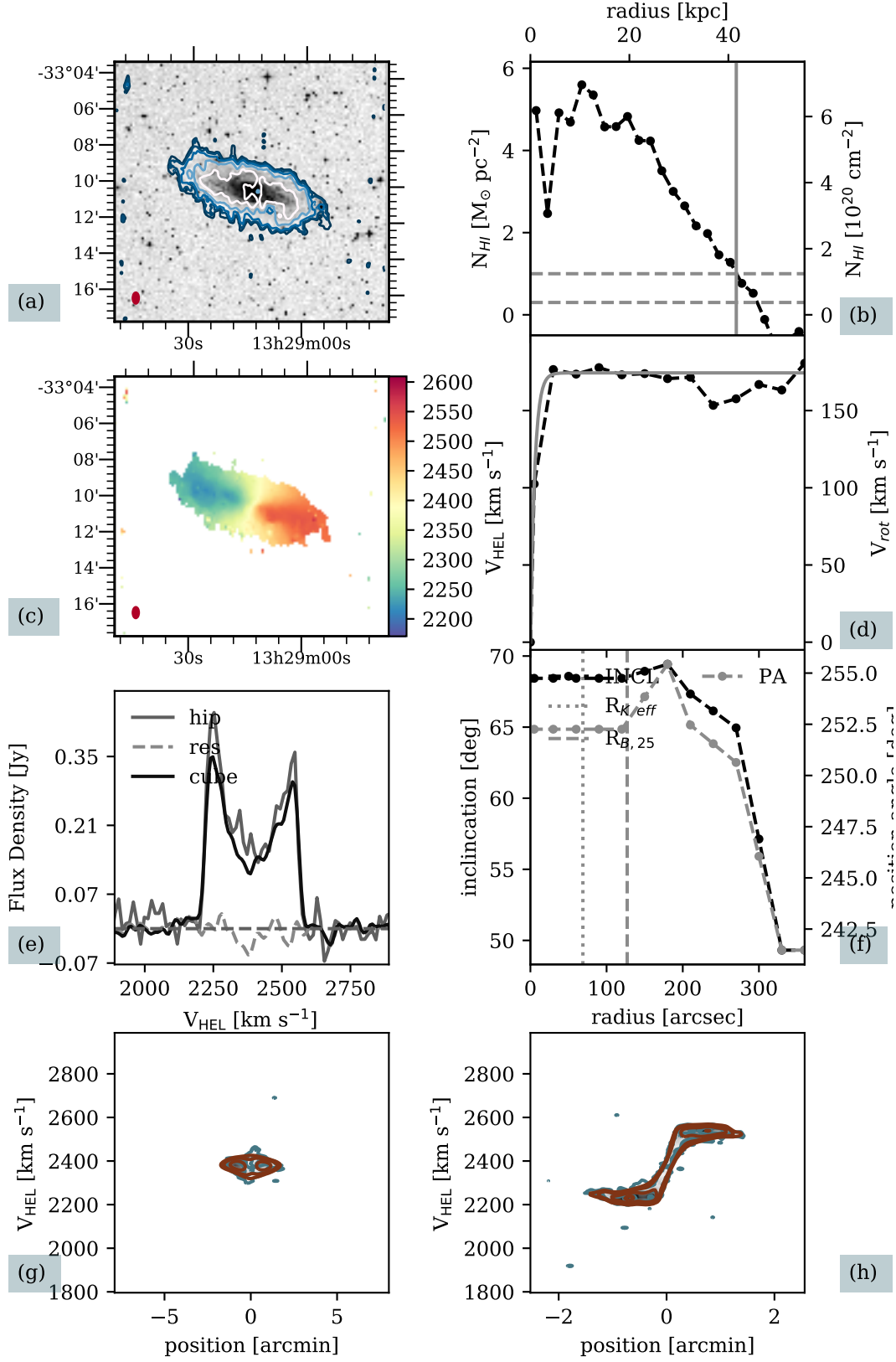


Figure B7. NGC5161

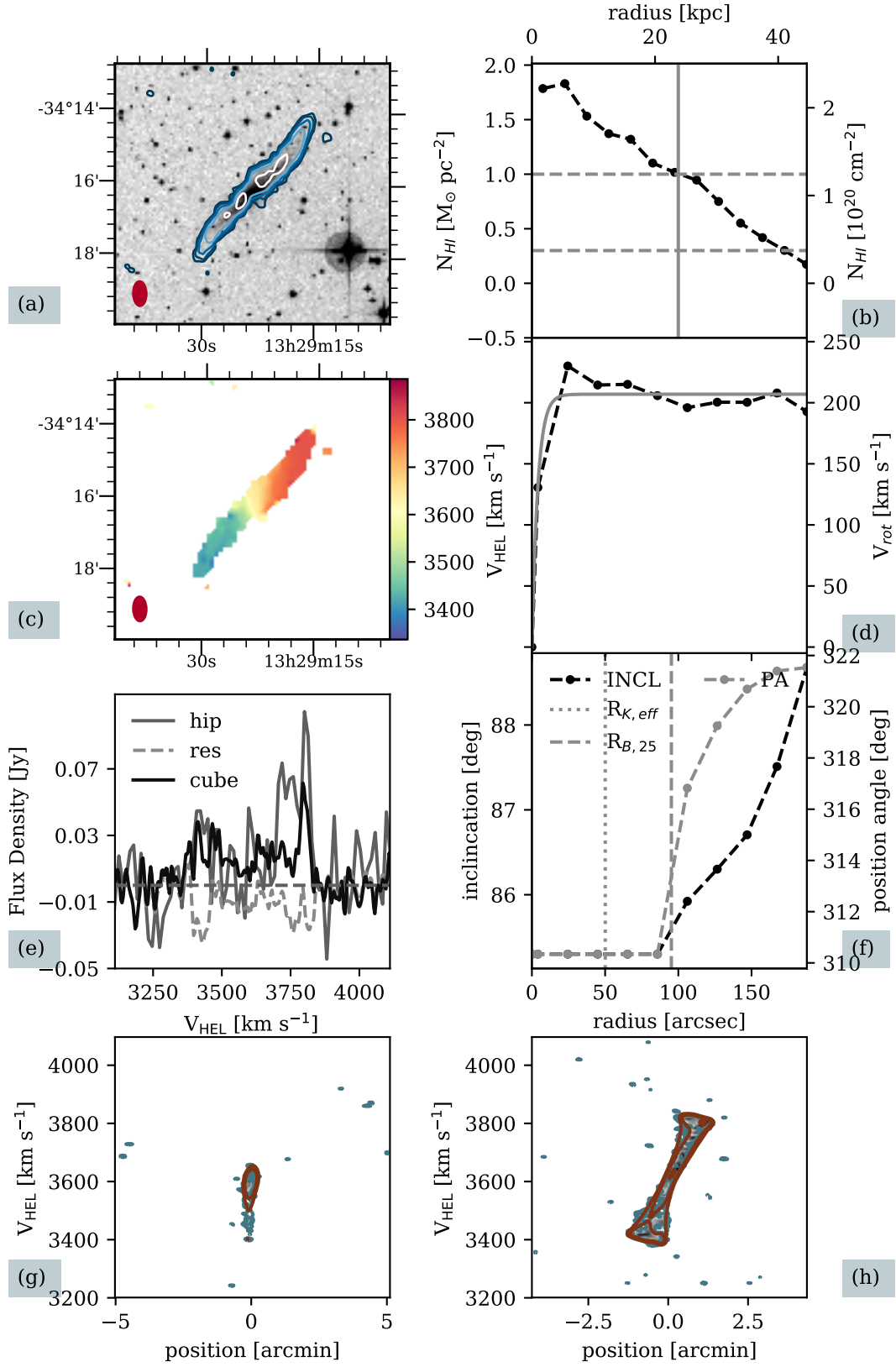


Figure B8. ESO383-G005

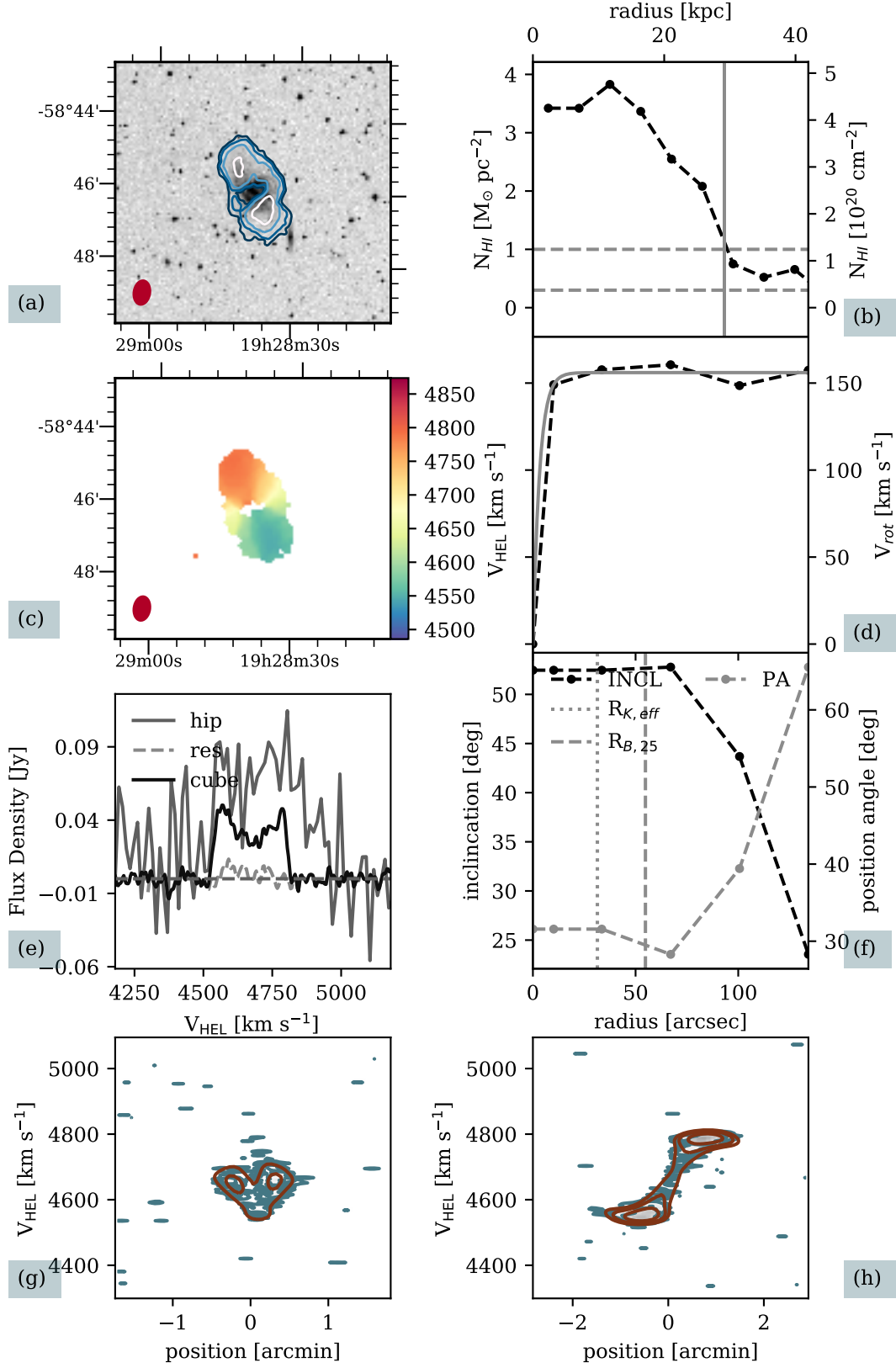


Figure B9. IC4857

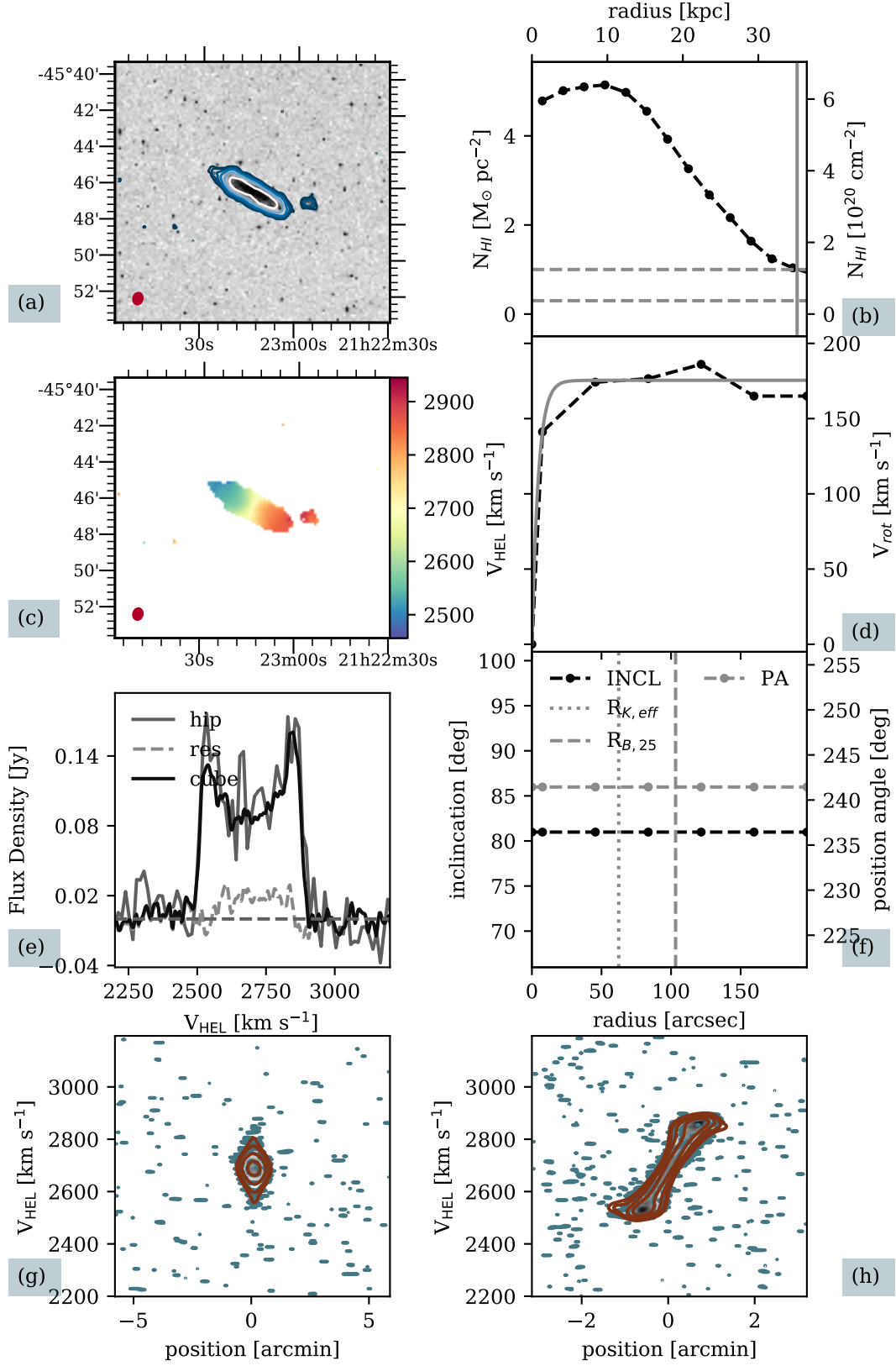


Figure B10. ESO287-G013

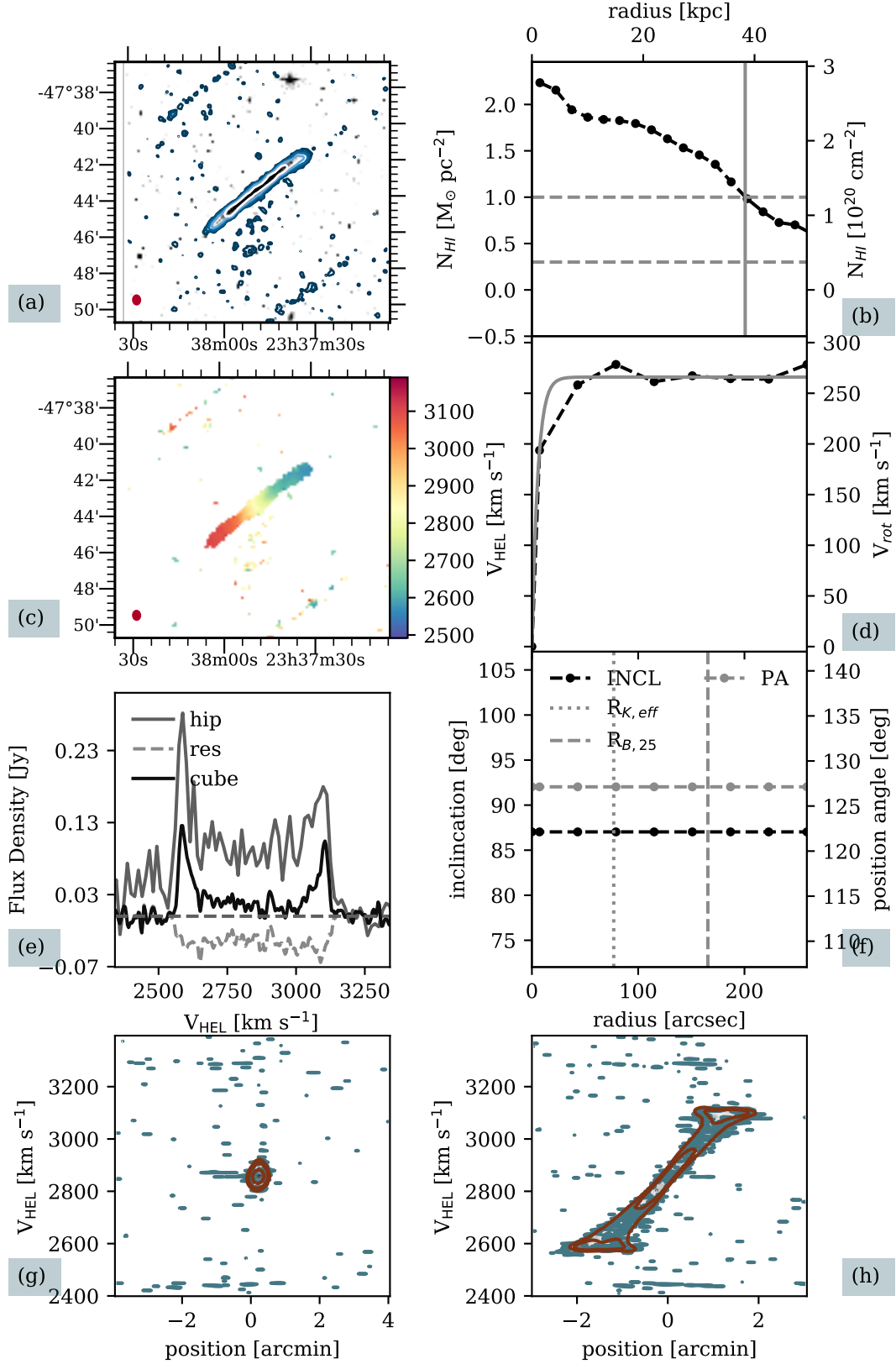


Figure B11. ESO240-G011